



A compact triband antenna using artificial magnetic conductor for wireless body area network communications

V. Rajavel¹ · Dibyendu Ghoshal¹

Published online: 28 April 2023

© The Author(s), under exclusive licence to Springer Science+Business Media, LLC, part of Springer Nature 2023

Abstract

The proliferation of the Internet of Things devices and advancements in wireless communication have fostered the growth of Wireless Body Area Networks (WBAN). This research provides a triband antenna supported by a 4×4 Artificial Magnetic Conductor (AMC) array surface that has a low Specific Absorption Rate (SAR), a high Front to Back Ratio (FBR), and increased gain for use in wearable devices. For WBAN communications, the proposed antenna operates in the Industrial, Scientific, and Medical (2.4 GHz) band, the C (3.7–4.2 GHz), and the Wi-Fi 6E (5.925–7.125 GHz) bands. The dual-band AMC unit cell exhibits Double-Negative and angular stability behaviour at 2.45 GHz and 6.5 GHz. AMC-backed antenna achieved multiband functionality by incorporating slots into the unit cell and a defective ground structure into the antenna. The antenna was positioned $0.139\lambda_0$ above the AMC surface, which measured $0.556\lambda_0 \times 0.556\lambda_0 \times 0.013\lambda_0$ (at 2.45 GHz). The antenna exhibited good gain and return loss variations when mounted on curved surfaces. The proposed integrated design yielded substantial enhancements, as evidenced by the increase of 8.2 dBi in maximum gain, 25.2 dB in FBR, and over 93% in total efficiency. The AMC-backed antenna's -10 dB impedance bandwidth is 18.4%, 21.2%, and 22.3%, with corresponding frequency ranges of 2.25–2.66 GHz, 3.66–4.53 GHz, and 5.9–7.35 GHz. Additionally, the AMC surface showed an average reduction in SAR of 93.22%. Vector Network Analyzer and Anechoic chamber measurements proved simulation accuracy. As a result, it is strongly recommended that the integrated antenna design be acknowledged in WBAN communications.

Keywords Triband antenna · WBAN communication · Artificial Magnetic Conductor · Specific Absorption Rate · Front-to-Back Ratio

1 Introduction

Modern wireless communications require high bandwidth, minimal latency, and fast data transfer. Compact and highly effective new microstrip antennas have been developed to meet the expanding needs of wireless communication systems. Remote employment and online education have become increasingly popular due to COVID-19 lockdowns, which have fostered a global shift in internet usage. There has been a significant shift in network traffic

from corporate and educational networks to mostly consumer broadband networks due to the worldwide spread of the COVID-19 epidemic. A robust and consistent connection must be linked to almost everything, from domestic appliances to traffic lights. The Internet of Things (IoT) is assisting businesses and workers in adapting to a more fluid work schedule in the wake of the pandemic. The availability of monitoring tools and the flexibility to access from anywhere has simplified remote work considerably. Wi-Fi enables the IoT to develop because of its secure and dependable connection [1]. The IoT is revolutionising the healthcare industry and many other aspects of our daily life. The IoT and wearable technology have significantly and positively impacted the business world and modern culture.

Wearables provide many new opportunities in the pharmaceutical and healthcare industries [2]. The

✉ V. Rajavel
rajavelece.sch@nita.ac.in; rajavel572@gmail.com
Dibyendu Ghoshal
tukumw@gmail.com; dibyendughoshal.ece@nita.ac.in

¹ Department of ECE, National Institute of Technology Agartala, Agartala, Tripura, India

emergence of wearable technology is reshaping finance and accounting processes, operations, and models, resulting in new consumer value, improved efficiency, and additional revenue streams. Wearable medical technology connected to the internet is a potential lifesaver. They help understand the patterns and symptoms of any health problem, physical or mental. Patients can play an active role in their treatment regimens and monitor their progress towards recovery in real-time with the help of internet-connected medical wearables [3]. Regulators must provide additional spectrum for Wi-Fi to continue driving IoT innovation despite network strain. High-definition media and the IoT are hindered by the slow download speeds of today's wireless networks. Therefore, the Wi-Fi Alliance introduced the Wi-Fi 6E standard. Users can find 802.11ax characteristics and capabilities in Wi-Fi 6E, and it does so in the 6 GHz range [4]. Additionally, to the 2.4 GHz and 5 GHz bands already supported, Wi-Fi 6E will enable the operation of features in the unlicensed 6 GHz frequency. Wi-Fi 6E's bandwidth is 5.925–7.125 GHz, with 14×80 or 7×160 MHz channels [5].

IoT-enabled medical wearables give users access to more accurate data about their health. Researchers are very interested in wearable antennas because of their potential impact on on-body wireless communications [2]. Consequently, the growth of Wireless Body Area Networks (WBAN) [6–9] and the need for wearable wireless devices is rising in a variety of fields, such as fitness trackers, healthcare tracking and monitoring systems [10], and military tracking systems [11]. The authors researched thoroughly before designing a flexible, small antenna backed by Artificial Magnetic Conductor (AMC) surface that may be utilized in WBAN applications using the newest Wi-Fi frequencies (Wi-Fi 6E). The C-band, classified by the Institute of Electrical and Electronics Engineers (IEEE) as the microwave frequency range between 4 and 8 GHz, primarily operates from 3.7 to 4.2 GHz and is designated by the Federal Communications Commission (FCC) in the United States (US). This band is widely used for satellite communications, wireless devices, cordless phones, and even some RADAR and weather RADAR systems, making it an essential part of modern communication technology. A circularly polarized quad-band antenna with four frequency bands and a large axial ratio bandwidth is described in [12]. The antenna comprises an L-shaped radiator, ground stub, and a rectangular strip on the opposing side and supports Wi-Fi 6E, 5G n77 and n78 frequency ranges. Two compact dual-band antennas have been proposed for WiMAX and Industrial, Scientific, and Medical (ISM) use [13]. As a result of AMC integration, the radiation properties of both antennas have been enhanced. An AMC-supported wearable antenna measuring $33 \times 33 \times 6.75$ mm³ and operating from 2.9 to

12 GHz was developed in [14]. AMC implementation leads to a reduction of 85.3% in the antenna's measured Specific Absorption Rate (SAR) value. A 1×2 textile-based AMC array measuring 50.7 mm \times 25.7 mm is utilized to improve the performance of a compact monopole antenna measuring 50 mm \times 20 mm [15]. The antenna has a realized gain of 6.76 dBi and an overall efficiency of 88.4% at its designated operating frequency of 2.45 GHz, making it ideal for Wi-Fi data transmission. A wideband rectangular-ring textile antenna is integrated with an AMC plane to enable operation in the frequency range of 6.78–8.77 GHz, as reported in [16].

A monopole antenna with a defective round type partial ground and 2×2 unit cells is merged with an AMC surface exhibiting Mu-Negative (MNG) characteristics and polarization-independent behaviour [17]. A 2×2 AMC array with L-slots in each unit cell is developed for a 2.45 GHz WBAN application [18]. The antenna exhibits an S_{11} of less than -15 dB, a Front to Back Ratio (FBR) greater than 20 dB, and a SAR of less than 0.15 W/kg, achieving good performance in the ISM band. A patch antenna with many slots for wearable and conformal applications has been developed [19]. Polyethylene Terephthalate (PET) was a substrate for 5.8 GHz, 6.2 GHz, and 8.4 GHz frequency ranges. Triangular slotted monopole antennae with a 4×4 AMC surface operate in the ISM and WiMAX bands [20]. The SAR has decreased by 99% thanks to the AMC surface. A staircase pattern defective ground monopole antenna is developed for dual-band operation in the C band (4–8 GHz) and the International Telecommunication Union (ITU) band (8.01–8.5 GHz) [21]. Two dipole-like AMC designs have been proposed for the flexible meander bowtie antenna [22]. Substrate thickness and AMC separation distance are emphasized. A $30 \times 30 \times 0.2$ mm³ sized windmill-shaped antenna, designed to operate at 5.71–5.99 GHz, is integrated into a 2×2 AMC array [23]. A WBAN-compatible wearable antenna with a dual-layered construction was described in [24]. The antenna features slotted unit cells on a 2×2 AMC surface, offering a peak gain of 7.4 dB and E-field and H-field isolation of 54.87 dB and 22.91 dB, respectively, in the ISM band. An ultra-wide, dual-band antenna is proposed for wireless capsule endoscopy [25]. The antenna is usable in the Ultra-Wideband (UWB) low-frequency spectrum since its relative bandwidth is 30.3% at 1.4 GHz and 53.3% at 4.0 GHz.

The study describes designing and implementing a compact multiband antenna with a dual-band AMC that delivers high gain, low SAR, and high FBR for WBAN communication. A microstrip patch antenna in the shape of a gear wheel is used in the proposed design. The gear wheel antenna has 12 interconnected teeth that provide Wi-Fi 6E and C bands coverage. A 4×4 AMC array provides

back-end support for the antenna to reduce electromagnetic radiation. It has respectable SAR, FBR, Voltage Standing Wave Ratio (VSWR), and gain performance. The AMC provides the characteristics of Double Negative (DNG) material within the given range. The angular stability behaviour for Transverse Electric (TE)/Transverse Magnetic (TM) waves in an AMC is investigated as a function of incident angle. The maximum achievable gain increases to 8.4 dBi with a 17 mm separation between the antenna and AMC. The AMC integrated antenna offers impedance bandwidth of S_{11} less than -10 dB at 2.45 GHz (18.4%), 4.1 GHz (21.2%), and 6.5 GHz (22.3%), and high FBR values of 15.4 dB, 25.2 dB, and 16.3 dB, respectively, making it suitable for WBAN use. Additionally, the overall band radiation efficiency of over 93% ensures excellent performance. The antenna has been built and tested in free space, and SAR has been validated with human tissues in the ANSYS HFSS simulator.

The rest of this paper is structured as follows. The AMC and antenna designs are in-depth in sections II and III. Section IV analyses the antenna's radiation characteristics and SAR to verify the integrated antenna's performance under different conditions. Finally, section V has a conclusion and summary.

2 AMC design and analysis

2.1 AMC design

Antennas can utilize AMC surfaces to control electromagnetic wave radiation, enhancing gain and focused transmission. This section describes constructing and analyzing a dual-band slotted AMC unit cell. The structure and geometry of an AMC unit cell are depicted in Fig. 1, with dimensions of $0.179\lambda_0 \times 0.179\lambda_0 \times 0.013\lambda_0$ at 2.45 GHz. The unit cell is fabricated using an FR4 epoxy substrate with a metal bottom surface featuring a thickness of 1.6 mm, a relative permittivity of 4.4, and a loss tangent of 0.02. Dual wideband responses are produced by placing slotted patches inside an AMC structure consisting of a square outline patch with cut-offs in all four corners.

ANSYS HFSS was utilized with the Floquet port and master–slave boundary conditions to model the AMC unit cell's electromagnetic characteristics. The AMC unit cell is a Perfect Magnetic Conductor (PMC) at the resonant frequency region where the zero-degree reflection phase is reached. At 2.45 GHz and 6.5 GHz, the proposed unit cell has a zero-degree reflection phase. Figure 2a and b depict the proposed unit cell reflection responses, and optimized parameters are displayed in Table 1.

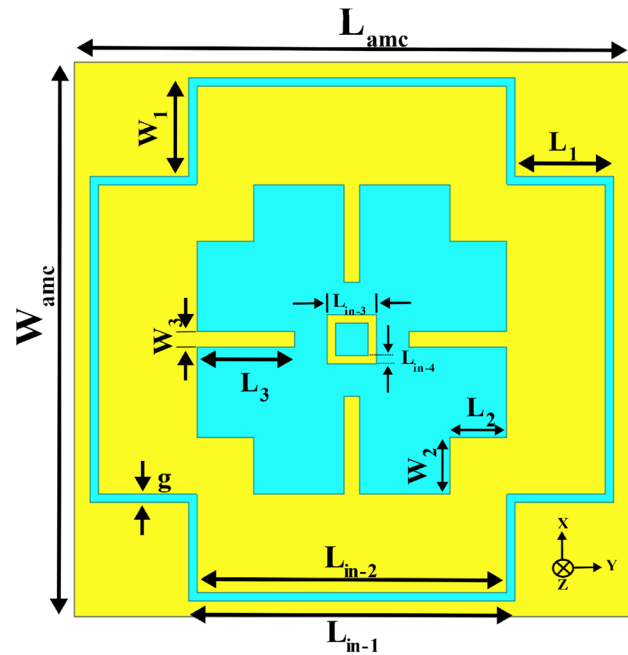


Fig. 1 Front view of the proposed unit cell

2.2 AMC evolution

The proposed AMC unit cell has undergone four stages of evolution, and Fig. 3 presents a detailed exposition of its development with emphasis on the various stages. The first stage, depicted in Fig. 3a, involves the creation of an AMC-1 square patch with $W_1 \times L_1$ size cut-offs on all four corners. At 2.45 GHz, AMC-1 has given a zero-degree reflection phase. The square patch with cuts of $W_2 \times L_2$ in all four corners is developed in AMC-2 to provide a dual-band reflection response. At 2.45 GHz and 7.3 GHz, the AMC-2 exhibited a zero-degree reflection phase, as seen in Fig. 3b. All sides of the AMC-2 inner square patches have $W_3 \times L_3$ size slots in AMC-3, as shown in Fig. 3c. In order to accommodate the Wi-Fi 6E band, it is essential to relocate the second zero-degree reflection phase to around 6.5 GHz. The zero-degree reflection response has been shifted to 6.7 GHz. AMC-3 unit cell has been modified to include square slots of the L_{in-3} size with a gap of L_{in-4} , which reduces the second zero-degree reflection response from 6.7 to 6.5 GHz. Figure 3d depicts the unit cell's final design, referred to as the AMC-4. Figure 4 depicts the simulation results of reflection phase responses at the various stages of design development.

2.3 AMC Parametric study

The reflection phase performance of the proposed AMC unit cell depends on four important parameters. They are the width of the outline patch 'g', the width and length of

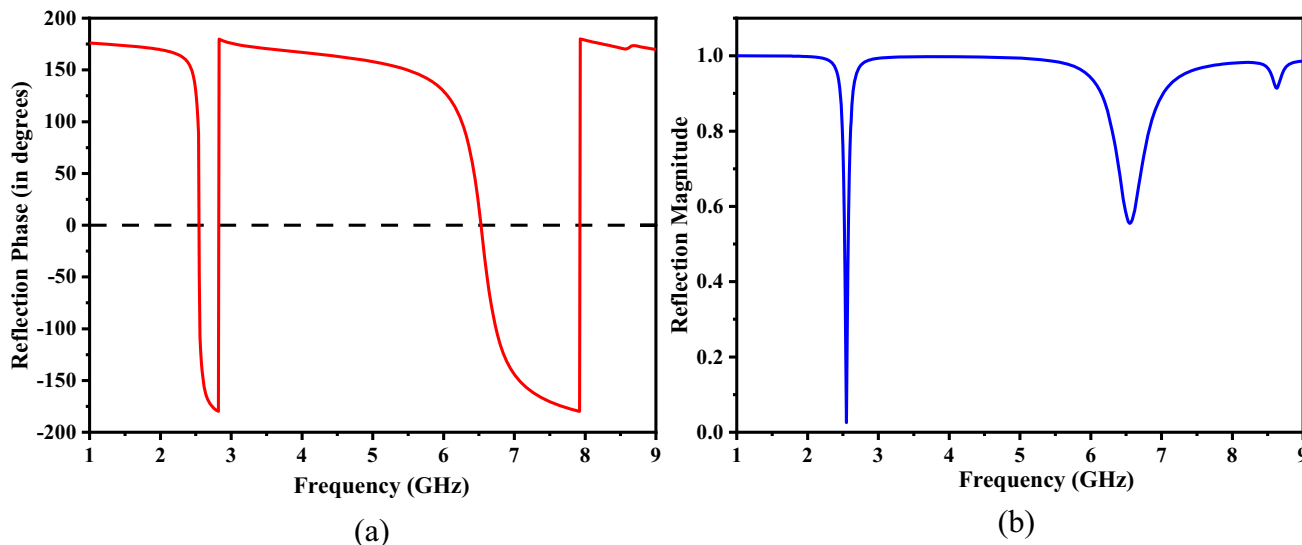


Fig. 2 Proposed AMC unit cell reflection responses **a** Phase **b** Magnitude

Table 1 Optimized design parameters of dual-band AMC unit cell

Parameters	Value (mm)	Parameters	Value (mm)
W_{amc}	17	L_2	1.75
L_{amc}	17	L_{in-3}	1.5
L_{in-1}	10	L_{in-4}	1
L_{in-2}	9.5	$g \ \& \ W_3$	0.5
W_1	3	L_3	3
L_1	3	W_2	1.75

the inner patch’s rectangular slots ‘ W_3 ’ and ‘ L_3 ’, and the length of the square-shaped corner slots ‘ L_2 ’. Figure 5 depicts the zero-degree reflection phases for both the upper and lower frequency ranges. Figure 5a shows that changing the ‘ g ’ value from 0.5 to 4 mm decreases the lower resonant frequency from 2.83 to 2.45 GHz and increases the higher resonant frequency from 5.46 to 6.5 GHz.

The inner patch’s corner square slot length (L_2) is the second parameter which can vary between 0.5 and 3 mm. Higher resonant frequency shifts from 6.04 to 7.09 GHz as L_2 increases, while lower resonant frequency stays at 2.45 GHz. Figure 5b shows that the optimal value of L_2 is achieved at 1.75 mm. The variation in the width of the inner patch rectangular slots (W_3) from 0.25 to 2 mm has no impact on the lower resonant frequency at 2.45 GHz. Therefore, an optimal W_3 value of 0.5 mm is obtained, while Fig. 5c demonstrates a reduction in the upper resonant frequency from 6.71 to 5.95 GHz. The length of the rectangular slots on the inner patch (L_3) will increase from 1 to 3.5 mm. Although the lower resonant frequencies remain constant at 2.45 GHz, the higher resonant frequency has decreased to 6.2 GHz. The unit cell with an L_3 of 3 mm contains the required frequency band. A variation in the reflection response curve concerning L_3 is seen in Fig. 5d.

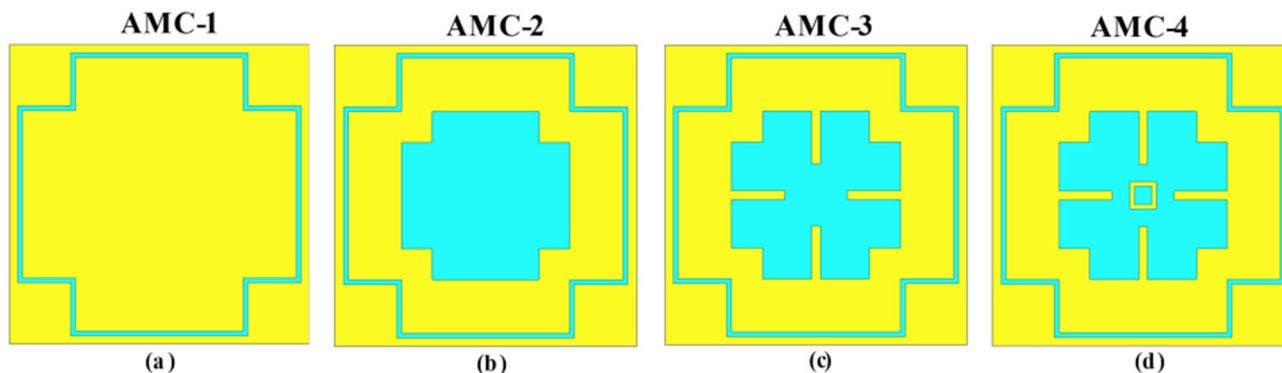


Fig. 3 Unit cell design stages **a** AMC-1 **b** AMC-2 **c** AMC-3 **d** AMC-4

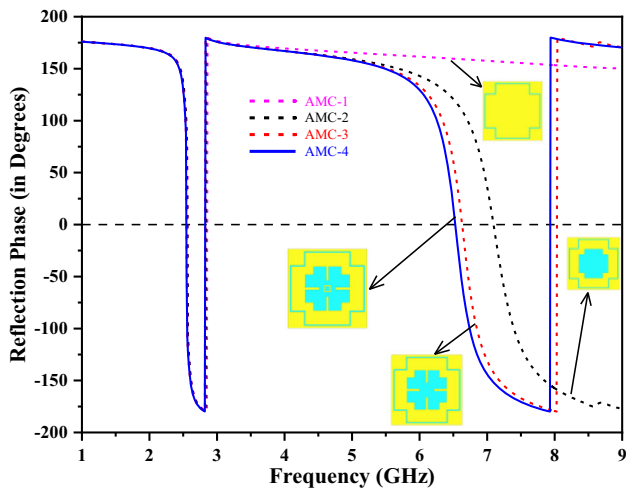


Fig. 4 Reflection phase responses of AMC-1, AMC-2, AMC-3 and AMC-4

2.4 AMC characteristics

The optimal material parameters for a unit cell’s structure can be determined using scattering parameters. By simulating the unit cell with a master–slave boundary condition in ANSYS HFSS, the scattering parameters can be obtained. The permittivity (ϵ), permeability (μ), refractive index (n), and impedance (z) of the material were determined using Eqs. (1) and (2) [26]. The multiplication of ‘k’ and ‘d’ represents the physically relevant optical path length. Permittivity and permeability are correlated with refractive index and impedance. The retrieved permittivity and permeability are shown in Fig. 6a and b, while the refractive index and impedance parameters are shown in Fig. 6c and d. The real values of permittivity and permeability at a frequency of 2.45 GHz are -1.8 and -1.5 , respectively. The refractive index at 2.45 GHz is -1.63

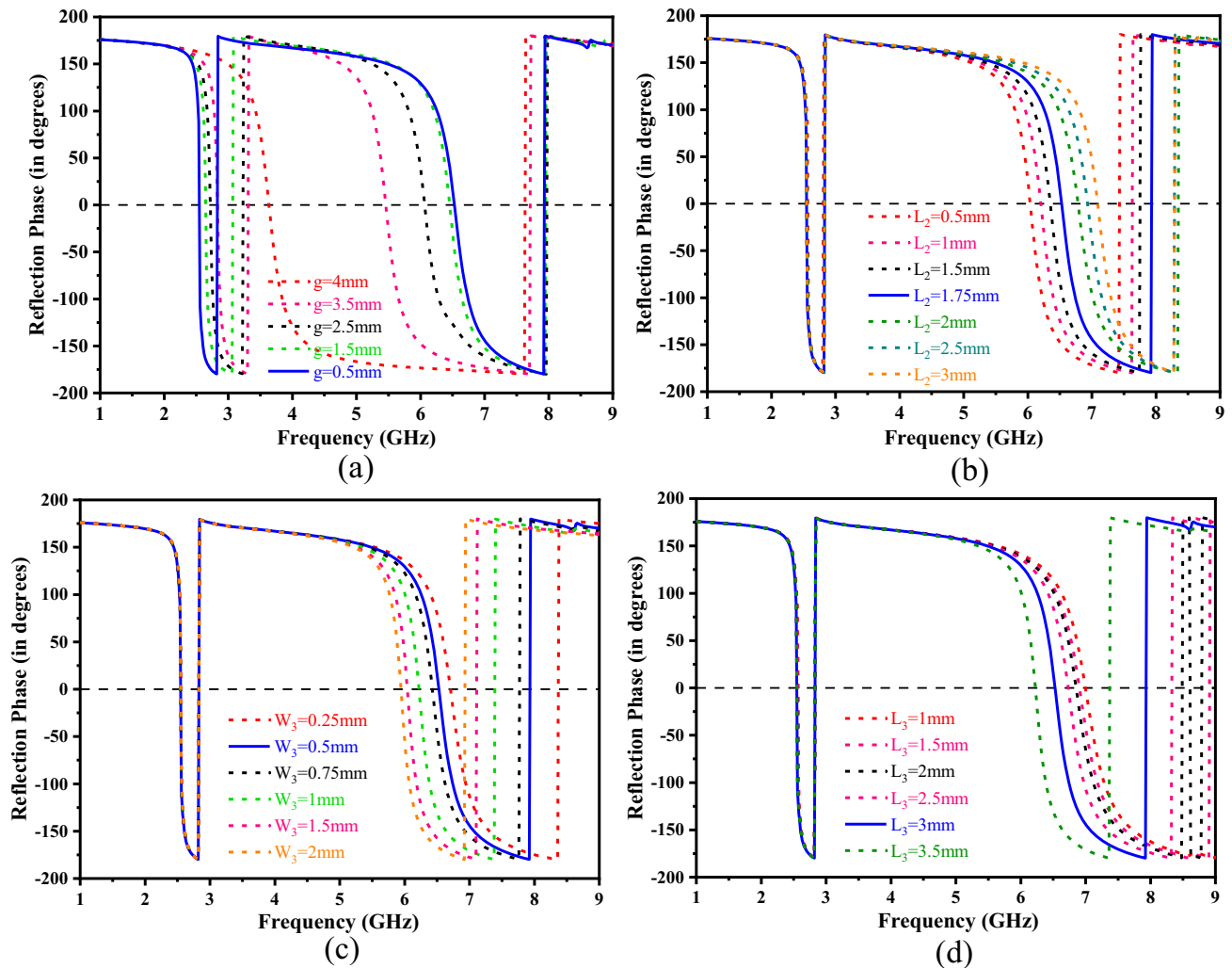


Fig. 5 Reflection phase variations of AMC unit cell a ‘g’ variation b ‘L₂’ variation c ‘W₃’ variation d ‘L₃’ variation

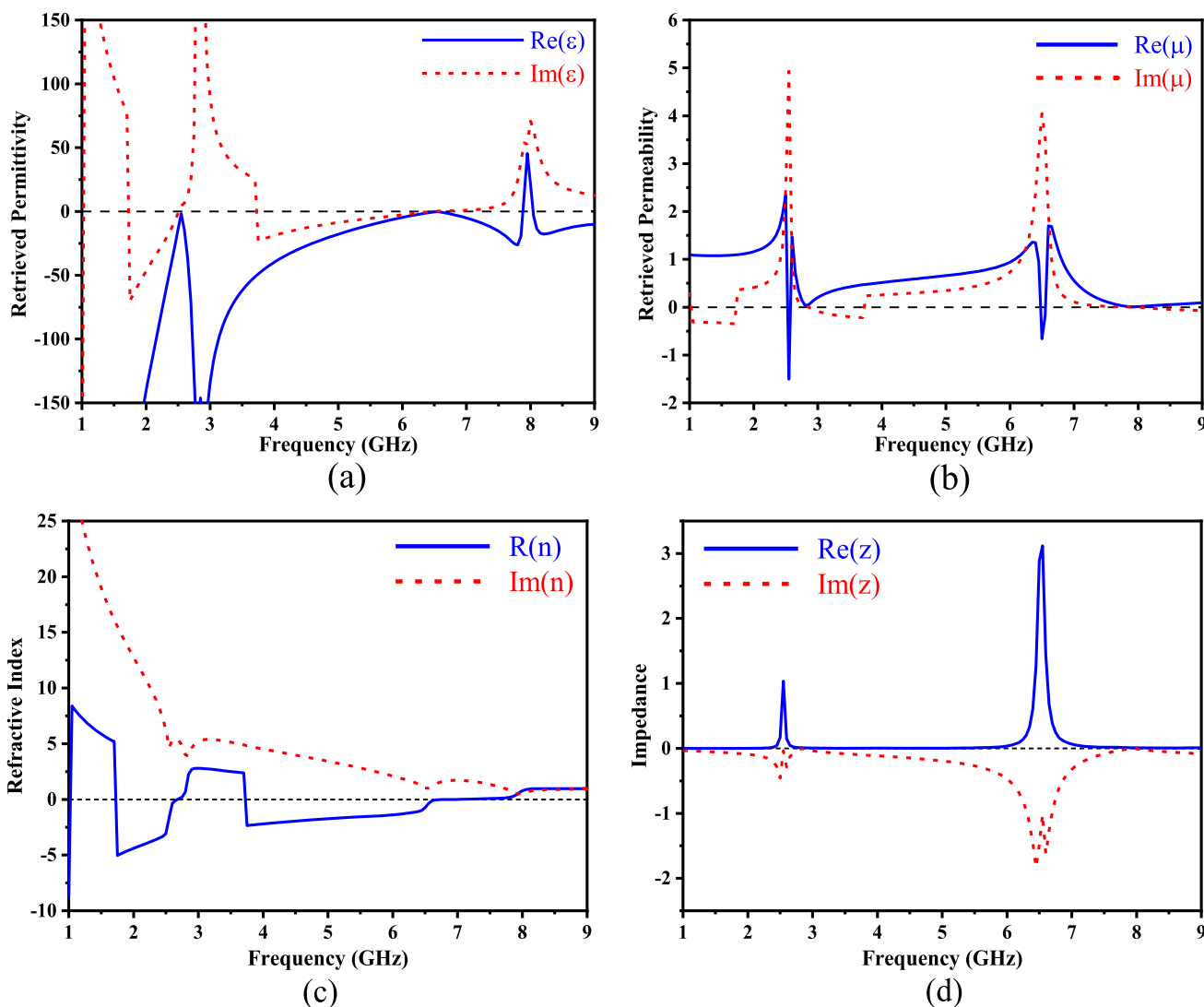


Fig. 6 Unit cell material parameters a Permittivity b Permeability c Refractive Index d Impedance

+ 4.7i, while the normalized impedance (z) value is 1.02–0.04i, falling within the range of free space impedance. According to Fig. 6, the unit cell gives significant positive wave impedances and a negative index of refraction that can be seen. The proposed AMC unit cell exhibits DNG characteristics and functions as a PMC by operating at the specified resonant frequency.

$$n = \frac{1}{kd} \cos^{-1} \left[\frac{1}{2S_{21}} (1 - S_{11}^2 + S_{21}^2) \right] \tag{1}$$

$$z = \sqrt{\frac{(1 + S_{11})^2 - S_{21}^2}{(1 - S_{11})^2 - S_{21}^2}} \tag{2}$$

2.5 Reflection phases for different angle of incidence

Angular stability is critical for the AMC to function as a flat ground plane beneath the antenna. As long as the unit cells are symmetric, AMC is polarization independent for waves with varied orientations. Zero-degree reflection frequency points of TE and TM waves at various incidence angles are shown in Fig. 7a and b. The behaviour of TE and TM polarized waves is analyzed to investigate the constancy of the zero-degree reflection point for both waves across the lower and higher resonant frequency points. The lower band zero-degree reflection point for both waves increase from 2.45 to 2.61 GHz as the incidence occurs between 0° and 180°. The zero-degree reflection points for incidence angles between 0° to 80° and 180° to 110° are identical. When the incidence angle

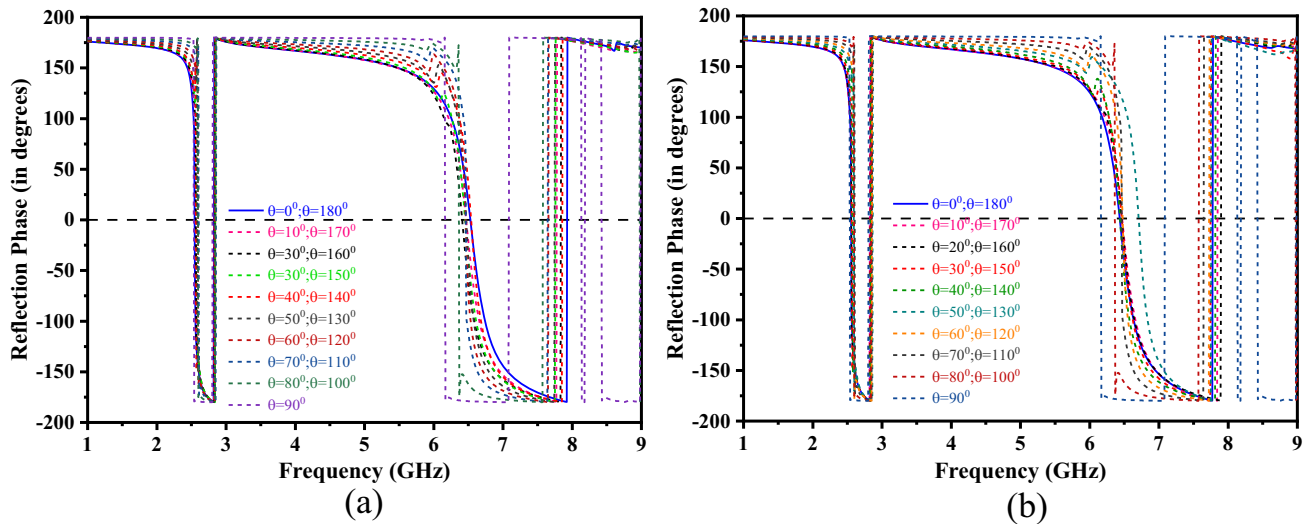


Fig. 7 The AMC surface’s simulated reflection phase under various incidence angles **a** for TE waves **b** for TM waves

increases, the upper band zero-degree reflection point for TE waves drops from 6.5 to 6.36 GHz. However, the zero-degree reflecting point for TM waves increases to 6.71 GHz for 45° and decreases to 6.43 GHz for angles 50° to 80°. Lower band zero-degree reflection points are 2.54 GHz, and 2.6 GHz for 90° incidences, and upper band zero-degree reflection points are the same for both waves.

2.6 AMC unit cell equivalent circuit model

The resonant nature of an AMC restricts its operating frequencies to a restricted band, resulting in frequency dependence. The resonance frequency of a design depends on the shape and dimensions of the structure as well as the thickness and relative permittivity of the substrate. An AMC can be represented as an LC network when the unit cell is smaller than the operating frequency wavelength [27]. Resonant frequencies have large surface impedances, and in-phase reflection bandwidths are proportional to \sqrt{LC} . L and C are the equivalent inductance and capacitance of the periodic unit cell and are used in Eq. (3) to calculate the resonant frequency (f_r). The unit cell’s resonance frequency decreases as its inductance or capacitance increases. Moreover, an increase in capacitance decreases the bandwidth. As a result, increasing the unit cell’s inductance rather than its capacitance is recommended. Using a thick substrate can increase the inductance without increasing the capacitance. Figure 8 illustrates that the resonant frequency corresponds to the effective equivalent circuit model [28].

$$f_r = \frac{1}{2\pi\sqrt{(L_g + L_d)C_g}} \tag{3}$$

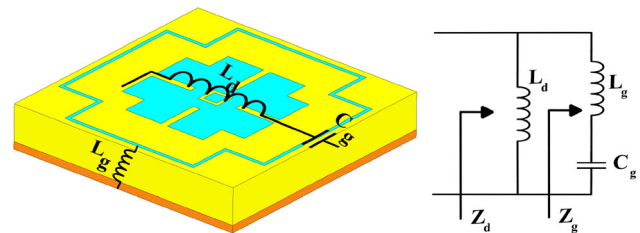


Fig. 8 Equivalent Circuit Model

A dielectric slab’s inductance is expressed as L_d , and grid inductance is expressed as L_g . The grid capacitance (C_g) between two parallel patches equals the distance between them. C_g and bandwidth will be calculated using the formulae in [28]. Adding parasitic patches and slots to the AMC shape alters the current patch, increasing the grid inductance L_g , as indicated by Eq. (3). L_d can be increased by Eq. (3) to raise the profile. The four-corner notch capacitance and inductance effects are essential in obtaining broad bandwidth. The authors are trying to maximise the shunt capacitance C_g to increase the device’s bandwidth and reduce its size simultaneously. Consequently, slot integration may regulate the resonance frequency and enhance AMC unit-cell performance.

3 Gear wheel shaped antenna design and analysis

3.1 Antenna design

This study describes an antenna optimized for Wi-Fi 6E and 2.4 GHz ISM band operation, including the 3.7–4.2 GHz C band, which can be utilized by WBAN

devices to achieve high-performance wireless connectivity. This article proposes an antenna design inspired by the gear wheel, a familiar mechanical component. An antenna's size is determined by considering the available space, wavelengths, and operational frequencies during the design process. The antenna is $36 \times 43 \times 1.6 \text{ mm}^3$ in terms of overall length. Three individual layers make up the proposed antenna when seen from the bottom to the top. Initially, a metal base plane is used as defected ground structure, followed by an FR4 epoxy substrate with a 1.6 mm thickness, a relative permittivity of 4.4 and a loss tangent of 0.02 widely accessible at a reasonable cost. There is a radiating patch on the top. When designing the antenna, the authors initially intended to cover only the Wi-Fi 6E and 2.4 GHz ISM bands, but it has now been expanded to include the C band (3.7–4.2 GHz). Table 2 illustrates the appropriate antenna parameters, and Fig. 9 shows the antenna from both the front and back. Parasitic patch components and a partial ground plane are used in this investigation to increase the antenna's radiation performance. The gear wheel antenna consists of two circular patches joined by six vector joints in the shape of rectangles. The gear wheel has 12 teeth arranged in a circular pattern around its outer edge. Inner vector joints and teeth of the antenna are intended to be of the same width to maximize radiation performance.

3.2 Antenna evolution

The evolution of the antenna design is discussed in this section. Figure 10 depicts the gear wheel-shaped dual-band antenna development in four stages. Regarding the evolution of antennas, they all have a standard size and material. Figure 11 compares the return losses of all antennas, which is crucial in determining their characteristics and performance. The progression begins with the conventional circular microstrip patch antenna. Figure 10a shows the traditional circular patch antenna initially designed for the 2.4 GHz frequency band. The circular patch antenna's dimensions were estimated using [29]. The circular patch antenna with a reflection coefficient of less than -10 dB

between 2.22 and 2.66 GHz was designated Antenna-1. In Antenna-1, two new circular slots have been added to accommodate a new working frequency band, as shown in Fig. 10b. Antenna-2 operates in the frequency ranges of 2.4–3.20 GHz and 4.17–5.8 GHz. The two slots in Antenna-2 are connected using rectangular-shaped vector joints to shift the second operational frequency to 6.5 GHz. Figure 10c depicts Antenna-3. Second-band in Antenna-3 now operates in a frequency range of 4.18–6.37 GHz. Meanwhile, the first frequency band is unaffected. Lastly, Antenna-3's outer circular patch is fitted with 12 teeth. Now, the second frequency covers both the Wi-Fi 6E band and the C band. Figure 10d depicts the final antenna design called Antenna-4, which operates in 2.2–4.5 GHz and 5.7–7.9 GHz.

3.3 Antenna parametric study

A parametric study of the gear wheel-shaped antenna is detailed below. As previously mentioned, the nature of an antenna can be determined by its reflection coefficient. The operating frequency of the gear-wheel-shaped antenna can be adjusted by adjusting the six key parameters. They are (1) the number of teeth of a gear wheel, (2) the number of vector joints, (3) the width of the gear wheel teeth ' W_t ', (4) the length of the gear wheel teeth ' L_t ', (5) width of the line feed ' W_f ', (6) substrate height ' Sub_H '. Figure 12 illustrates the comparison of the reflection coefficient of the antenna with various parameter variations. The number of teeth in the gear wheel can vary from 6 to 16, as shown in Fig. 13. Increasing the number of teeth increases the lower and upper operating frequencies. In the 14–15 teeth range, the values of the lower and upper bands' reflection coefficients are nearly identical, as shown in Fig. 12a. The ISM, C, and Wi-Fi 6E frequency bands are all accessible when using 12 teeth.

The number of vector joints is the second parameter to be considered. The number of vector joints might vary from 5 to 8. Figure 12b shows the reflection coefficient for each modification in the number of vector joints. The upper band response becomes narrower as the number of vector joints increases in this parametric study. The gear wheel-shaped antenna receives nearly identical responses with 6 and 7 numbers vector joints. The optimal number of vector joints found by the authors for achieving the best result with AMC was 6. The width (W_t) and length (L_t) of the gear wheel teeth are the following two parameters under consideration for parametric investigation. Figure 12c shows the gear wheel width ' W_t ' ranging from 1 to 3.5 mm with a 0.5 mm increment. The upper band response shows significant shifts due to variations in width between 1 and 2 mm. A variation of 2.5 mm to 3.5 mm significantly affects the lower band response. As a result, 2 mm is

Table 2 Optimized design parameters of the wheel-shaped antenna

Parameters	Value (mm)	Parameters	Value (mm)
$W_{\text{ant}} \ \& \ W_{\text{g}}$	36	L_{in}	5
L_{ant}	43	R_1	2
L_{g}	13	R_4	11
W_{f}	4	R_3	8.5
L_{f}	14	L_{t}	2.5
W_{t}	2	R_2	4

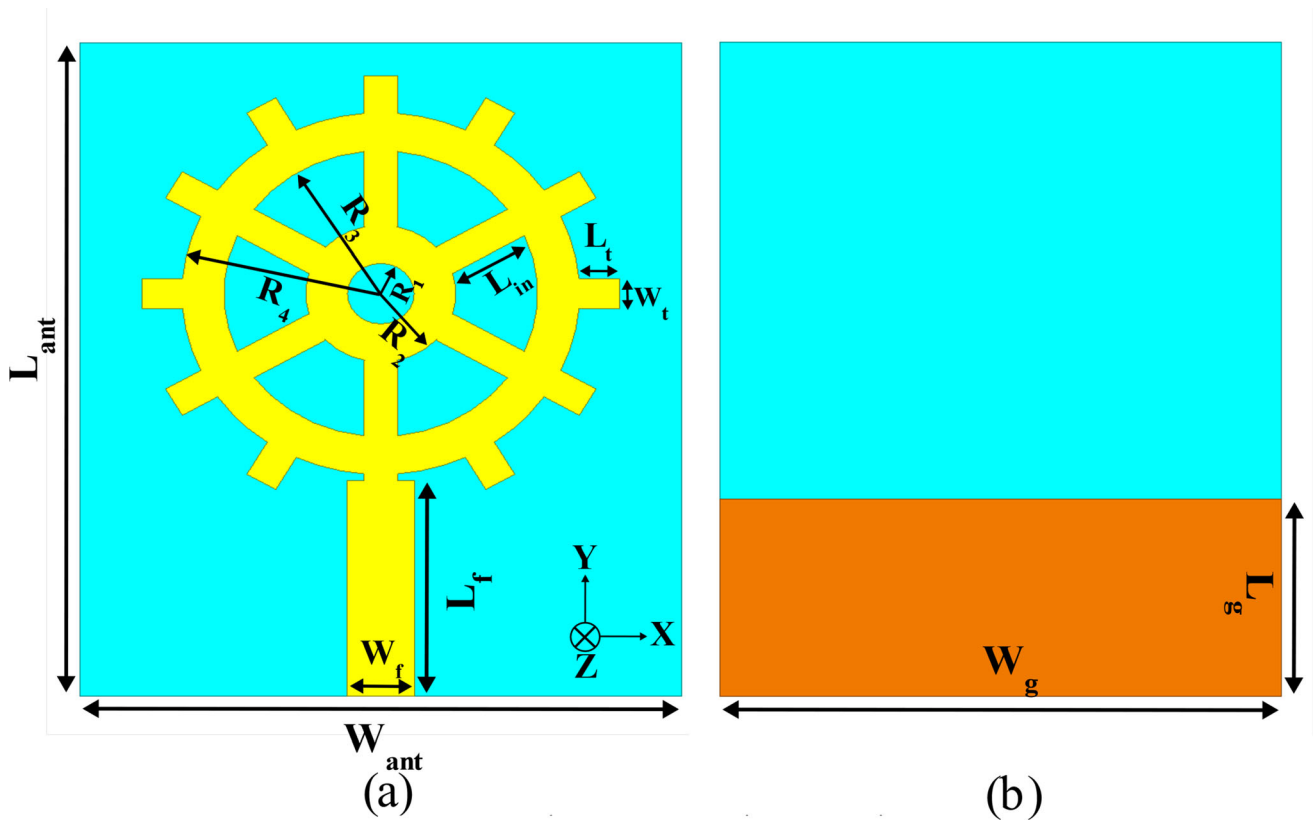


Fig. 9 Proposed antenna a Front view b Rear view

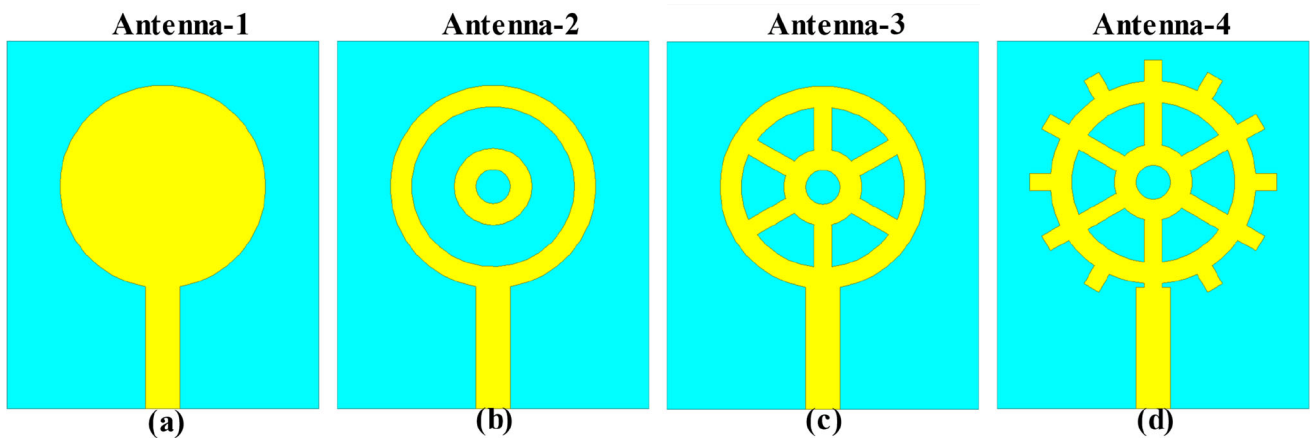


Fig. 10 Antenna design Evolution a Antenna-1 b Antenna-2 c Antenna-3 d Antenna-4

chosen as the optimal value for the width of gear wheel teeth. Like the last parameter, ‘ L_t ’ also varies from 1 to 4 mm. As the length of the gear wheel teeth increases, the upper band response also increases up to 5.5 GHz at a 3.5 mm variation, as illustrated in Fig. 12d. Improved results were found at 2.5 mm. The reflection coefficient response for the substrate height ‘Sub_H’ variation is shown in Fig. 12e. Substrate heights of 0.4 mm, 0.8 mm, 1.6 mm, and 2.5 mm are employed in the simulation

process, depending on the availability of the FR4 material in markets. A substrate height of 1.6 mm yields the best response. Feed line width is the final parameter considered for parametric analysis. W_f has seven variations, each with a 0.5 mm increment from 3 to 6 mm. Figure 12f illustrates that the antenna exhibits responses in the lower and upper bands for different widths of the feed line. An antenna having a W_f value of 4 mm exhibits more excellent

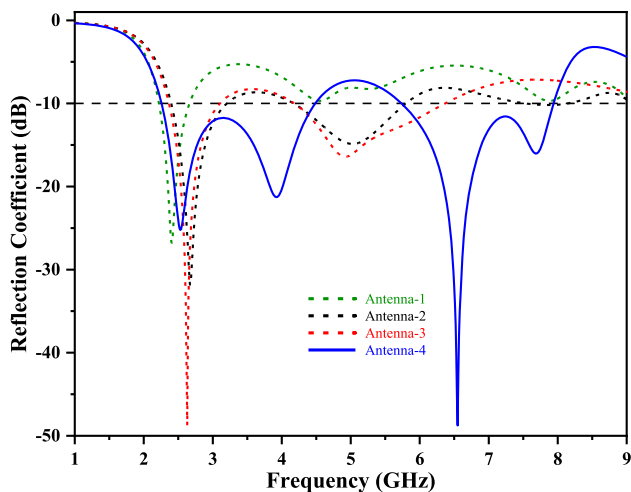


Fig. 11 Reflection Coefficient comparison of Antenna-1 to Antenna-4

responsiveness at frequencies of 2.45 GHz, 4.1 GHz, and 6.5 GHz.

3.4 Performance of Antenna

The dual-band antenna proposed in this study was fabricated from FR4 material with a thickness of 1.6 mm. Figure 14a shows the bandwidths of the simulated reflection coefficients (less than -10 dB) from 2.26 to 4.49 GHz (66.07%) and from 5.74 to 7.94 GHz (32.16%). The lower resonating band includes both ISM and C bands. The simulated VSWR for the proposed antenna is shown in Fig. 14b. The simulated VSWR values are less than two across the frequency ranges of 2.24–4.53 GHz and 5.68–7.96 GHz. The simulation results for radiation patterns in XZ and YZ planes are depicted in Fig. 15. In the 2.45 GHz, 4.1 GHz, and 6.5 GHz frequency bands, the proposed gear wheel-shaped antenna exhibits a spherical and omnidirectional radiation pattern. Figure 15a–c illustrates the radiation patterns at 2.45 GHz, 4.1 GHz and 6.5 GHz, respectively. Figure 16 presents both the front and rear perspectives of the fabricated antenna.

4 Integrated design simulation and measurement results

The gear wheel-shaped antenna radiator can operate as an electromagnetic reflector when positioned with a gap of $0.139 \lambda_0$ (foam_H) between itself and the AMC plane. Antenna radiation parameters in free space and human proximity are discussed along with bending analysis in this section.

4.1 AMC-backed antenna measurements in free space

The radiation performance of the proposed antenna with the AMC is verified by fabricating and measuring a prototype. The fabricated gear wheel-shaped antenna with AMC surface is seen in Fig. 17. The antenna and AMC surface are fabricated independently before being physically joined together. An air gap is created between the antenna and AMC by using Styrofoam. At the first resonance frequency, the antenna has overall dimensions of $0.556\lambda_0 \times 0.556\lambda_0 \times 0.165\lambda_0$ with a 4×4 unit cell. The VSWR and S-parameters of the antenna were evaluated using a Vector Network Analyzer (VNA). Figure 18 illustrates the antenna measurement setup in the Anechoic chamber. Figure 20a shows the antenna measurement in VNA. The VNA display screenshot of the S_{11} and VSWR results is depicted in Fig. 20b and c, respectively.

In contrast, the microwave anechoic chamber was used to test the radiating performance, including gain, radiation pattern, and radiation efficiency. Simulated S_{11} and VSWR with and without AMC and measured results are shown side by side in Fig. 19a and b. Simulations of the integrated antenna design demonstrate an impedance bandwidth of 18.4% (2.25–2.66 GHz), 21.2% (3.66–4.53 GHz), and 22.3% (5.9–7.35 GHz), with a reflection coefficient below -10 dB. Antenna S_{11} values below -10 dB were measured with AMC support in the frequency bands of 2.3–2.55 GHz (10.31%), 3.8–4.5 GHz (16.87%), and 5.86–8.24 GHz (33.76%). The measured VSWR values were less than two for frequency ranges of 2.48–2.64 GHz, 4.04–4.44 GHz, and 5.68–8.28 GHz. The measured bandwidth of the antenna is slightly narrower than the simulated bandwidth, which can be attributed to fabrication tolerances and the impact of SMA connector soldering (Fig. 20).

The FBR is a ratio that can be used to learn about the amount of energy reflected. However, there is a bound when considering the antenna's matching, realized gain, and FBR performance. The antenna's FBR is poor at 2.45 GHz, with a value of only 0.57 dB, but the integrated design improved performance by a significant 15.4 dB. Figure 21a also depicts the antenna FBR improvement at 4.1 GHz and 6.5 GHz. Antenna bandwidth, gain, and FBR are compared with and without an AMC surface in Table 3.

Figure 21b contrasts the antenna's realized gain with and without an AMC surface. The realized gain of the antenna varies between -20 dBi and 10 dBi within its operating frequency range. At 4.1 GHz, a gain of 8.2 dBi was observed. The simulated realized gain of the antenna is approximately 7.1 dBi, 8.2 dBi, and 7.5 dBi at frequencies of 2.45 GHz, 4.1 GHz, and 6.5 GHz, respectively. The

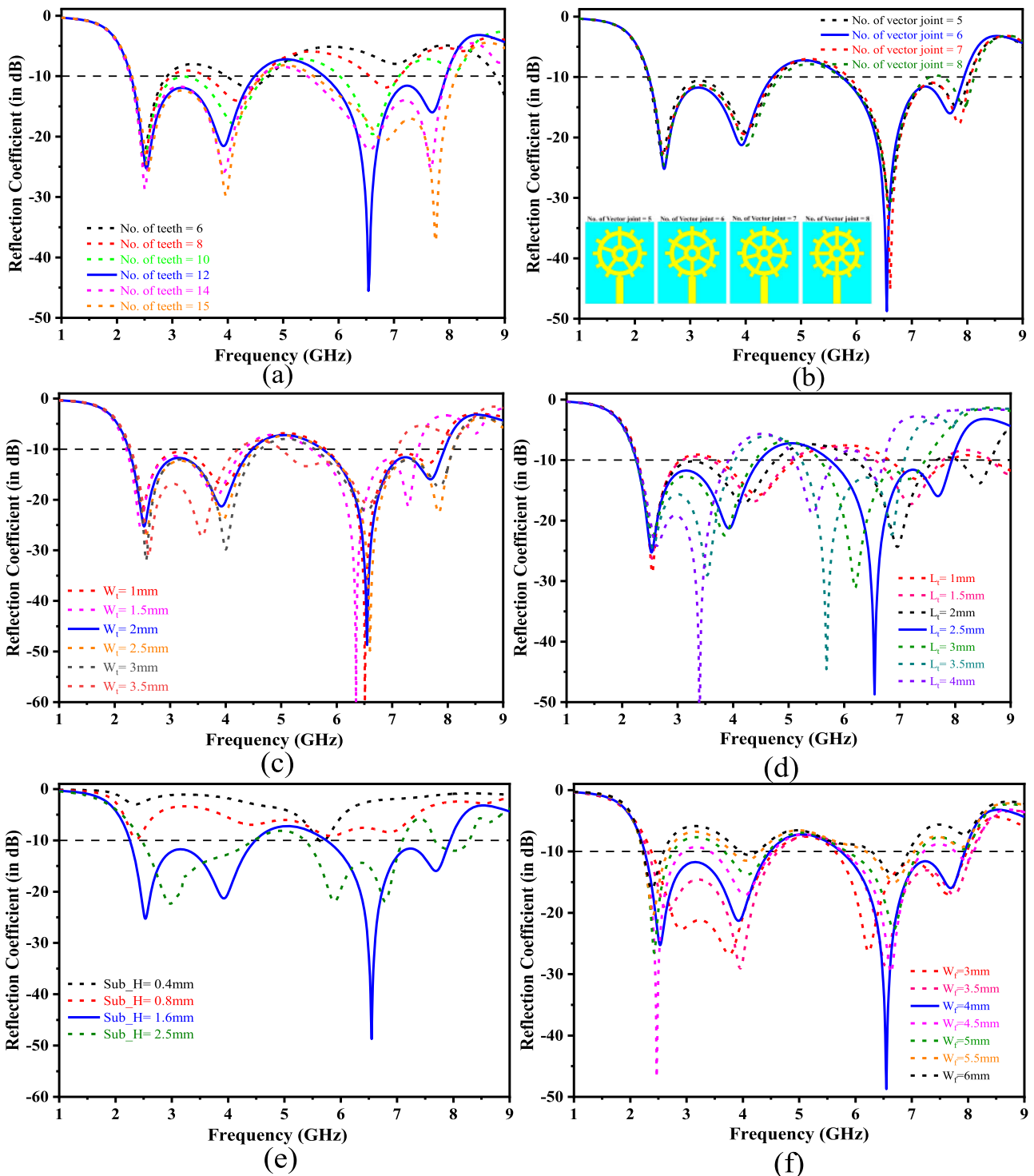


Fig. 12 Parametric analysis of the antenna **a** number of teeth **b** number of vector joints **c** ‘ W_t ’ **d** ‘ L_t ’ **e** ‘ Sub_H ’ **f** ‘ W_f ’

measured gains of the AMC-backed antenna are 4.69 dBi at 2.45 GHz, 10.54 dBi at 4.1 GHz, and 7.45 dBi at 6.5 GHz. Figure 21b presents a graphical representation of the measured and simulated gain of the antenna.

The radiation patterns were measured and simulated at 2.45 GHz, 4.1 GHz, and 6.5 GHz. The radiation pattern in the YZ plane of the antenna is symmetrical, while the radiation pattern in the XZ plane is Omnidirectional. The antenna’s radiation pattern is drastically altered by the

Fig. 13 Variation in number of teeth in gear wheel shaped antenna

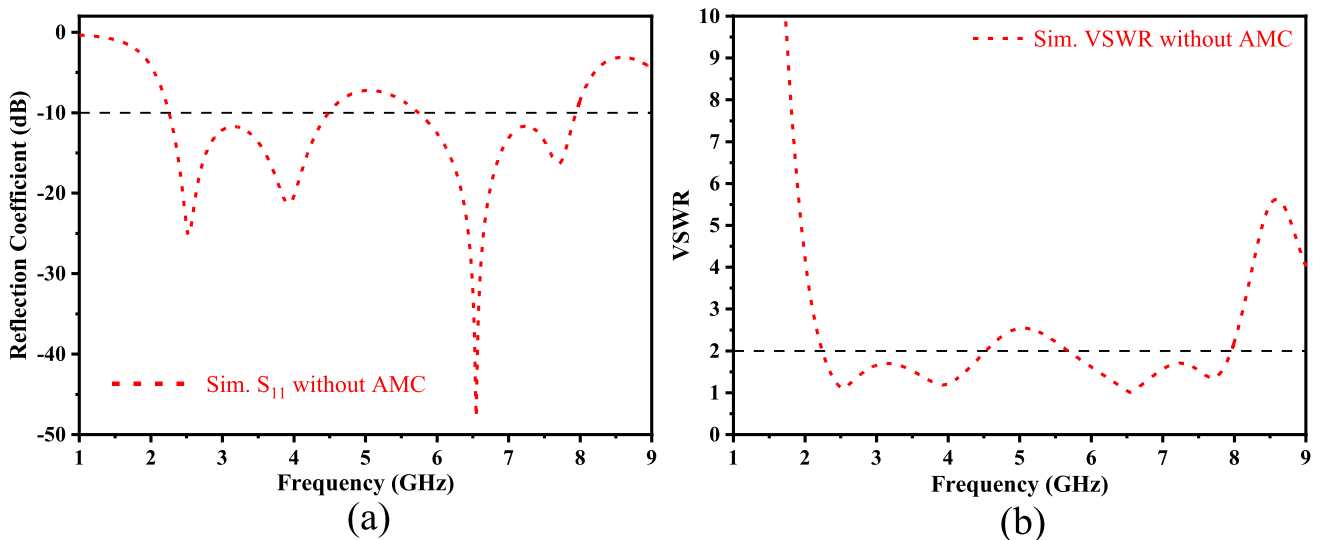
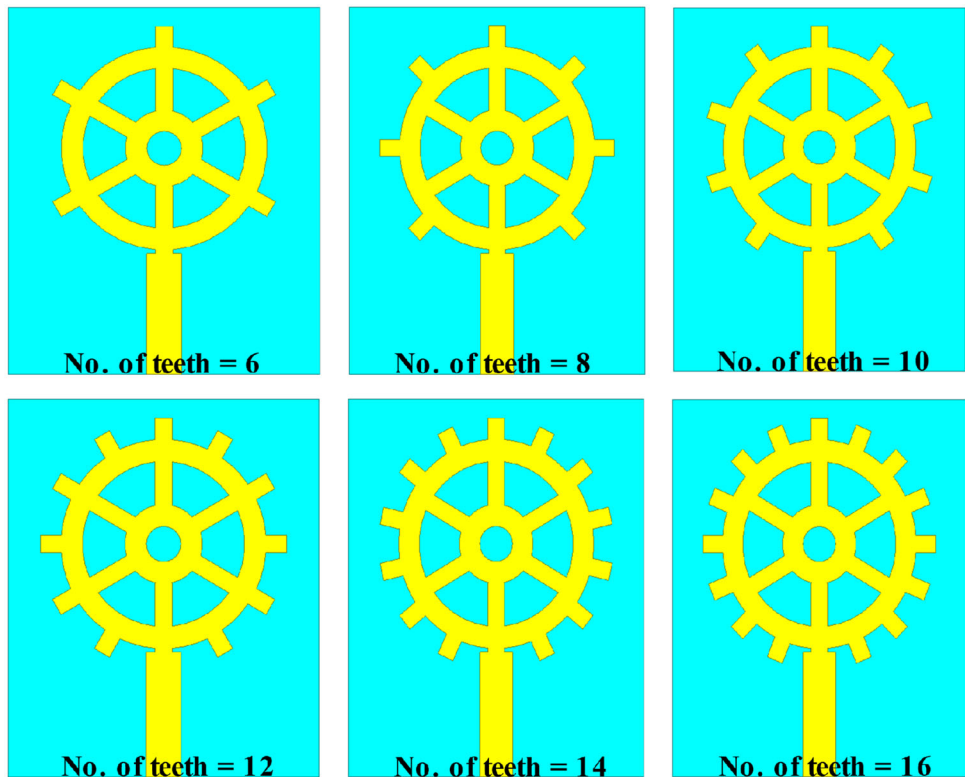


Fig. 14 Antenna parameters **a** S_{11} **b** VSWR

AMC structure, notably in terms of minimizing side lobes and enhancing directivity. Back lobe suppression is as high as 8.85 dB at 2.45 GHz, 9.26 dB at 4.1 GHz, and 5.46 dB at 6.5 GHz. At 4.1 GHz, the radiation pattern has a single side lobe. On all three frequencies, the measured findings match those from the simulations. The radiation patterns of the antenna at three operational frequency bands are depicted in Fig. 22, showcasing both the simulated and measured results.

4.2 Antenna with AMC analysis

The AMC-supported antenna was examined in three distinct scenarios. (1) for various AMC array sizes, (2) for varied distances between the antenna and the AMC structure, and (3) for different orientation angles.

AMC-backed antenna performance was examined for various AMC array sizes regarding the reflection coefficient and realized gains. Depending on the gear wheel-

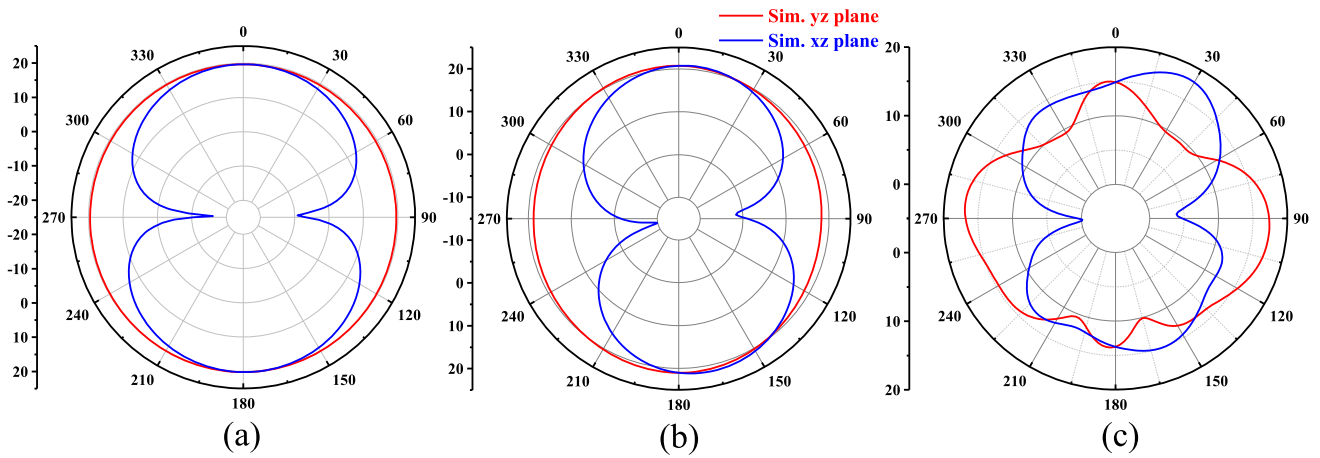


Fig. 15 Radiation Pattern **a** at 2.45 GHz **b** at 4.1 GHz and **c** at 6.5 GHz

Fig. 16 Fabricated antenna front view and back view

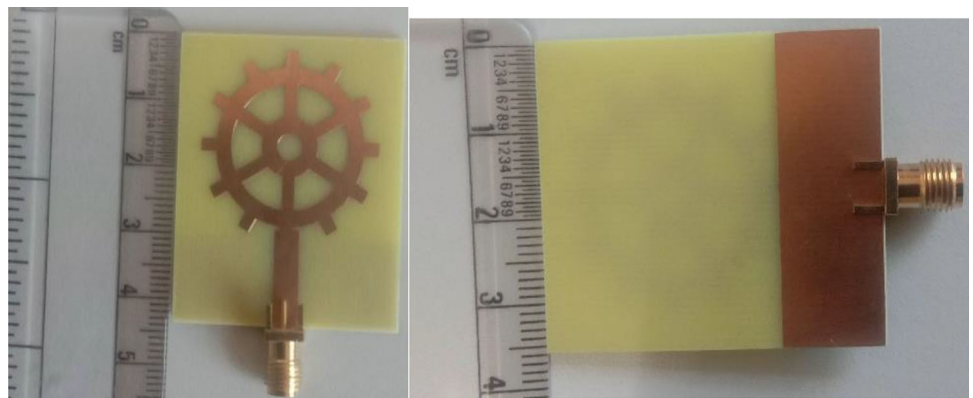
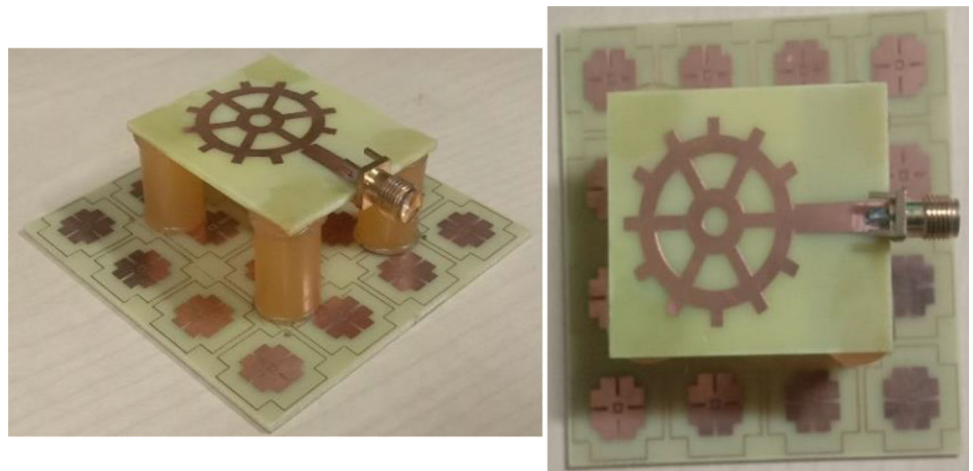


Fig. 17 Fabricated antennas with AMC: side and top view



shaped antenna parameters, the author may adjust the AMC array size from 3×3 , 3×4 , 3×5 , 4×3 , 4×4 and 4×5 unit cells. When the array size increases from 3×3 to 4×5 , the impedance bandwidth at the first resonant frequency of 2.45 GHz expands from 3.6% to 17.95%. In a 4×3 array, the bandwidth for the first resonating band is quite limited. The -10 dB reflection coefficient values are

achieving better performance in the third resonating band for all AMC array sizes except the 3×5 and 4×5 configurations. The 4×4 array size provides a large bandwidth in all the resonating frequency bands. Figure 23a illustrates the reflection coefficient for various AMC array sizes at resonant frequencies of 2.45 GHz, 4.1 GHz, and

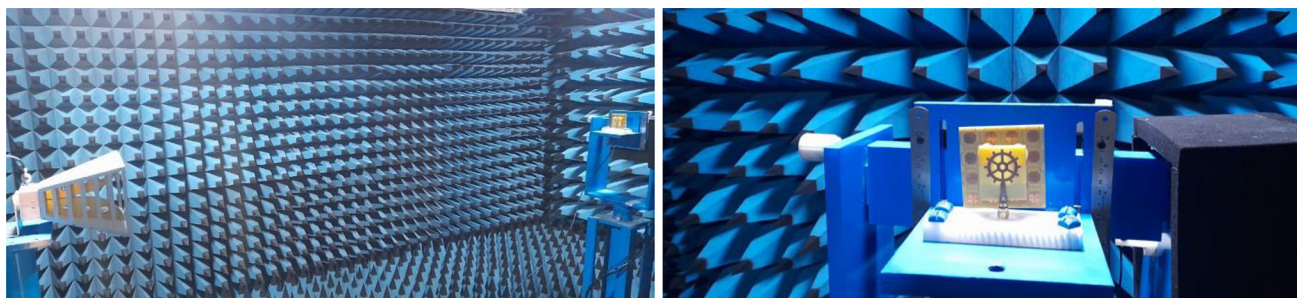


Fig. 18 Measurement setup of gear wheel shaped antenna with Anechoic Chamber

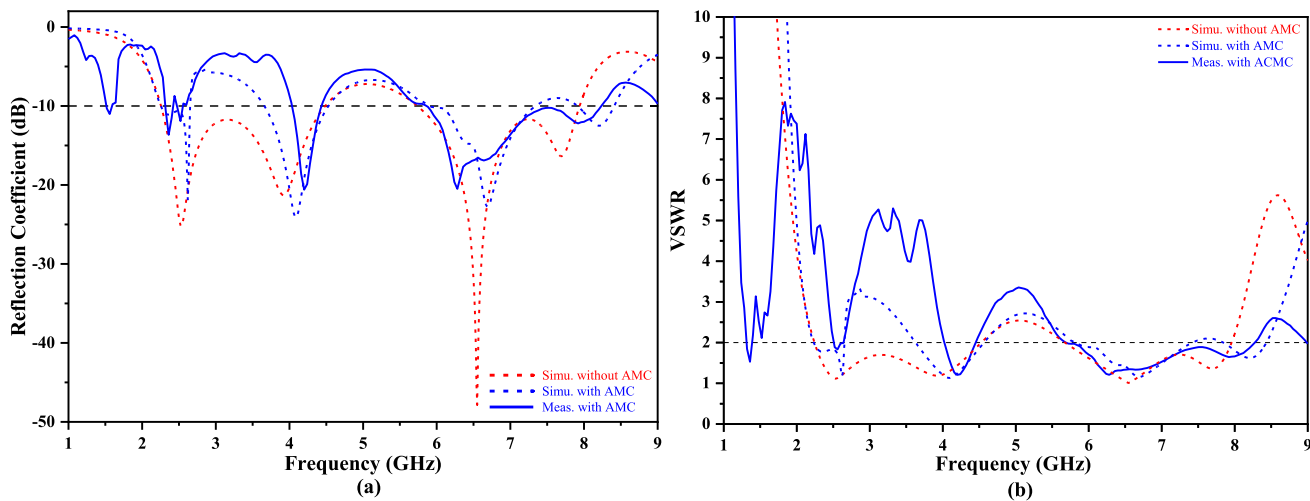


Fig. 19 Simulated and Measured results of antenna performance a S_{11} b VSWR

6.5 GHz, while Table 4 presents the realized gain data for the exact array sizes and frequencies.

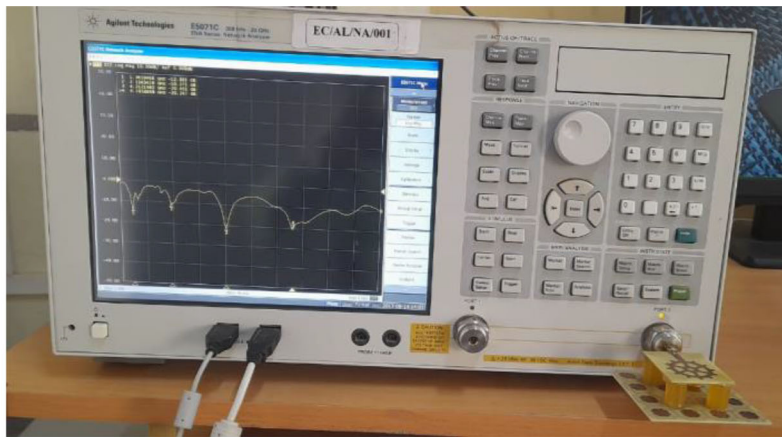
The antenna-to-AMC surface distance (foam_H) ranges from 13 to 18 mm. Figure 23b illustrates the impact of foam_H values on the S_{11} of an antenna with a 4×4 AMC surface. Figure 23b shows that when the distance between the antenna and the AMC surface increases, the bandwidth increases in all three resonating frequency ranges. The antenna's S_{11} achieves optimal performance at a foam_H value of 17 mm in all three resonant frequency bands. The S_{11} of the antenna exhibits excellent performance in the second and third resonating frequency bands at a foam_H value of 18 mm. Except for a foam_H value of 17 mm, the S_{11} performance of the antenna in the first resonating frequency band is subpar compared to other values. As a result, 17 mm has been chosen as the optimum distance between the antenna and the AMC.

The angle of rotation (or orientation) is a technical phrase that describes the angle between the antenna axis and the AMC surface. Figure 24a shows the antenna axis rotation with the AMC surface. The antenna is rotated over a range of angles from 0° to 90° . When the antenna is rotated at angles of 0° and 90° , the symmetrical surface of

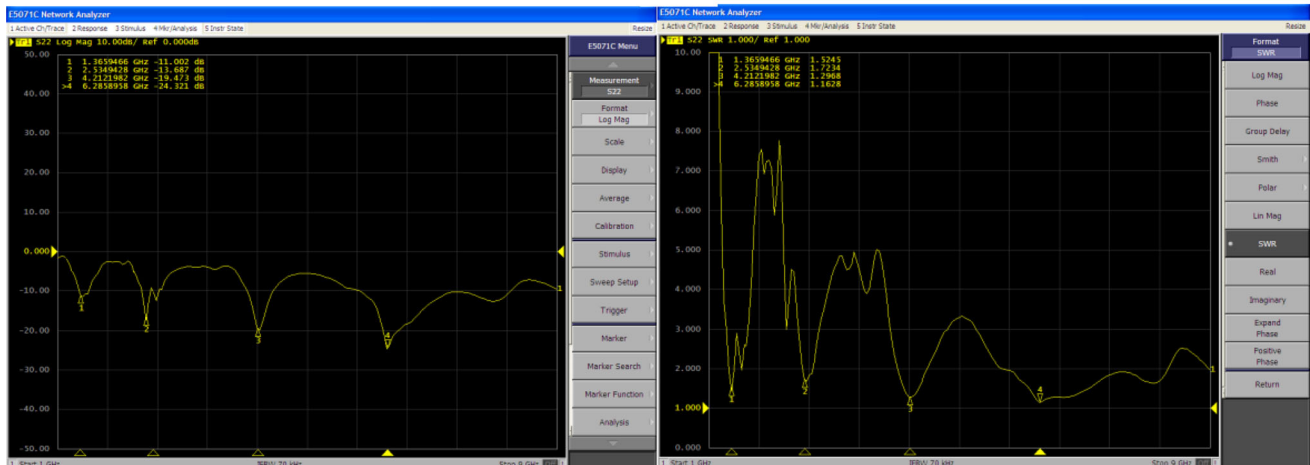
the AMC produces similar outcomes. The S_{11} performance of the antenna remains stable in each resonating band when the antenna is rotated between 10° and 80° , as shown in Fig. 24b. A rotation of 50° results in a low S_{11} of -23 dB in the first resonating band, while the impedance bandwidth in the second and third bands becomes narrower compared to other rotation angles in the same band. Antenna performance with AMC is best when rotated at a zero-degree angle.

4.3 Bending analysis

Wearable antennas are vulnerable to change due to the human body's posture and motion in real-world requirements, notably for WBAN applications. Therefore, it is crucial to investigate the impact of varying the bending angle of a wearable antenna in open space. Conformal simulations assess the antenna's return loss performance beneath a deformable surface. In this arrangement, the entire antenna is wound around a cylinder in the y-direction. Antenna performance is tested in various bending conditions by varying the cylinder radius from 30 to 150 mm. The cylinder is treated as an unmodeled entity in



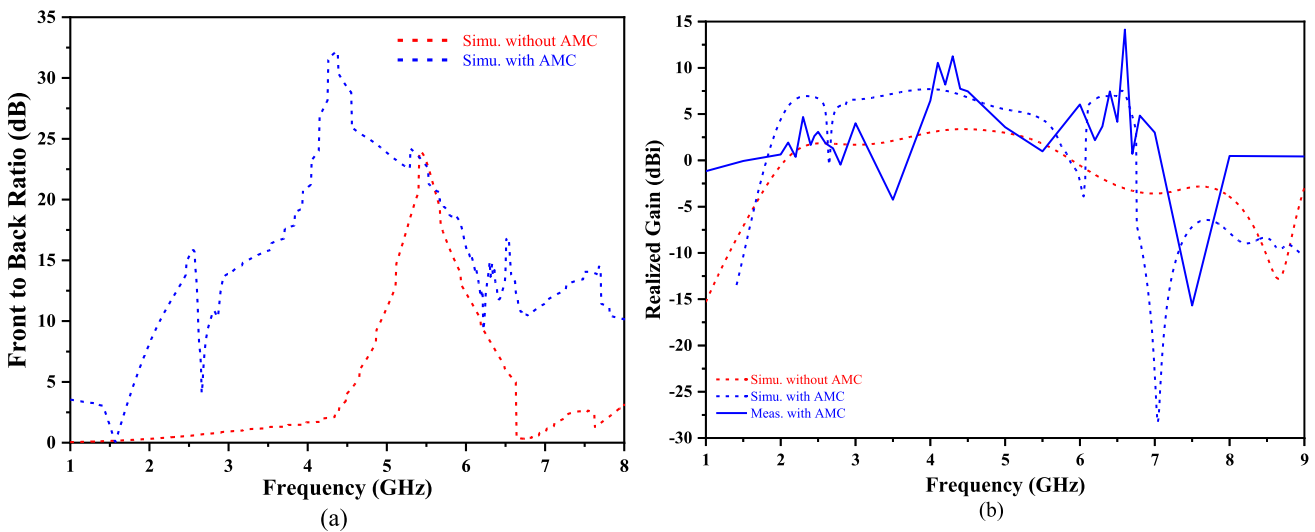
(a)



(b)

(c)

Fig. 20 a Measurement setup of antenna with Vector Network Analyzer b Screenshot of S_{11} results c Screenshot of SWR results



(a)

(b)

Fig. 21 a Simulated FBR of antenna with and without AMC b Simulated and measured results of realized gain of antenna

Table 3 Impact of AMC surface introduction on antenna performance

Resonant frequency band	Operating frequency (GHz) (S11 < - 10 dB)	S11 (dB)	- 10 dB impedance bandwidth (%)	VSWR (< 2) frequency range (GHz)	VSWR value	Gain (dB)	
1	Simulated without AMC	2.26–4.49	- 25.23	66.0	2.24–4.53	1.11	1.84
	Simulated with AMC	2.25–2.66	- 21.92	18.4	2.23–2.65	1.24	7.1
	Measured with AMC	2.3–2.55	- 13.65	10.31	2.48–2.64	1.78	4.69
2	Simulated with AMC	3.66–4.53	- 24.12	21.2	3.63–4.57	1.16	8.2
	Measured with AMC	3.8–4.5	- 20.60	16.87	4.04–4.44	1.23	10.54
3	Simulated without AMC	5.74–7.94	- 47.83	32.16	5.68–7.96	1.03	2.23
	Simulated with AMC	5.90–7.35	- 22.75	22.3	5.83–7.42	1.19	7.5
	Measured with AMC	5.86–8.24	- 20.49	33.76	5.68–8.28	1.33	7.45

this scenario. There are two situations where bending analysis is performed (with and without AMC surface). Return loss simulation results and screenshots of bending at 30 mm, 90 mm and 150 mm for a bent antenna without and with an AMC surface are displayed in Figs. 25 and 26, respectively. Bent antenna designs yield similar results to a straight antenna, with minor differences in reflection coefficient and bandwidth. When comparing the return losses under the bending and flat situations, it is clear that they are consistent with one another. It has been found that the antenna's return loss performance degrades significantly below a 30 mm bending radius. With a 60 mm bending, the reflection coefficient depth of the bent antenna increases from - 24 dB to - 32 dB at 2.45 GHz, while at 6.5 GHz, it decreases from - 50 dB to - 33 dB with a 120 mm bending.

The antenna was subjected to a bending experiment on an AMC surface. The bending and flat situations agree well when the antenna is 17 mm (foam_H) from the AMC surface. It has been found that the first resonating band narrows, and the third resonating band widens under considerable bending. Increasing the radius of curvature from 90 to 150 mm causes the first resonant bandwidth to widen and the third resonant band to narrow while the - 10 dB value rises to - 40 dB. The results of the bent antennas were comparable to those of the unbent antennas, suggesting that the bending did not significantly impact their performance. The S_{11} value is more affected by bending in small cylinders than in large ones due to the greater degree of bending. The increased size of the AMC sheet certainly makes antennae housed in AMC enclosures more prone to bending than those in non-AMC enclosures.

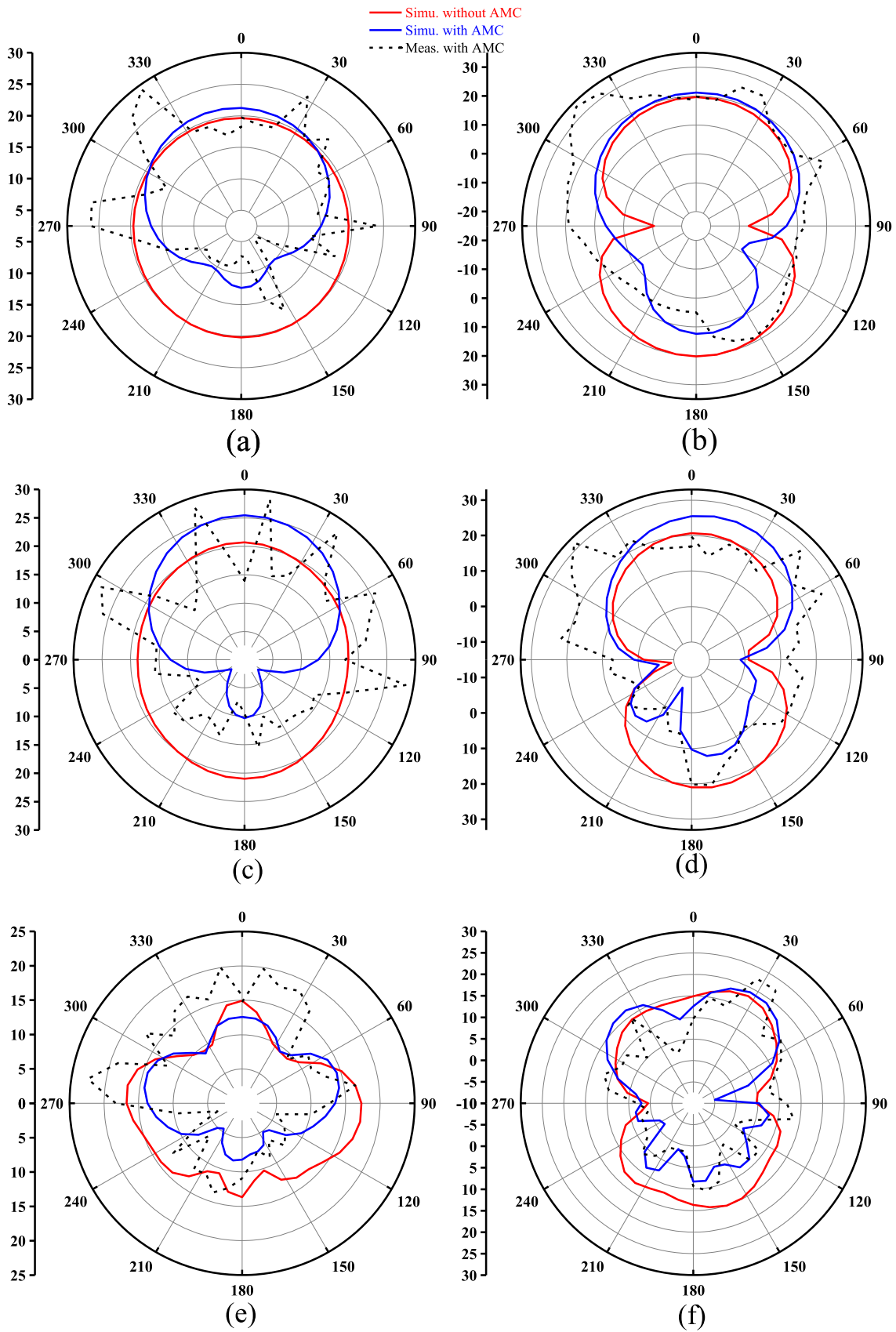
4.4 SAR analysis

The SAR is the standard for measuring the effect of electromagnetic radiation on living tissue. SAR is a crucial design parameter for ensuring the health and safety of individuals wearing antennas. The antenna's performance as a wearable device near human body tissue was assessed by examining it alongside a portion of a human phantom. The antenna's SAR values have been calculated using a human left hand, arm, and leg model in both the presence and absence of an AMC surface. A pre-existing human body and torso model could not be directly loaded into ANSYS HFSS due to the complexity of the model mesh and the compilation time.

The SAR can be determined using Eq. (4) [30]. Where \vec{E} , σ , and ρ are the electric field (in V/m), the tissue conductivity (in S/m), and the tissue mass density (in kg/m³).

$$SAR = \frac{\sigma |\vec{E}|^2}{\rho} \quad (4)$$

The human model's average SAR (in W/kg) is depicted in Fig. 27. The decision to set the distance between the antenna and human tissue at 5 mm was based on the complexity of the model mesh and compilation time constraints, as well as the need for a thorough understanding of the effects of electromagnetic radiation on human tissue. The US and European Union (EU) SAR limits of 1.6 W/kg and 2 W/kg are safe for human exposure. The SAR was calculated by averaging a volume encompassing each mesh point in the human phantom model. The SAR values were consistently below the maximum allowed by the standard.



◀Fig. 22 Antenna radiation patterns in the plane, both simulated and measured: a YZ at 2.45 GHz, b XZ at 2.45 GHz, c YZ at 4.1 GHz, d XZ at 4.1 GHz, e YZ at 6.5 GHz, f XZ at 6.5 GHz

According to the findings, the AMC successfully reduced the SAR levels at all three resonance frequencies. Material property changes make the AMC surface a high-impedance

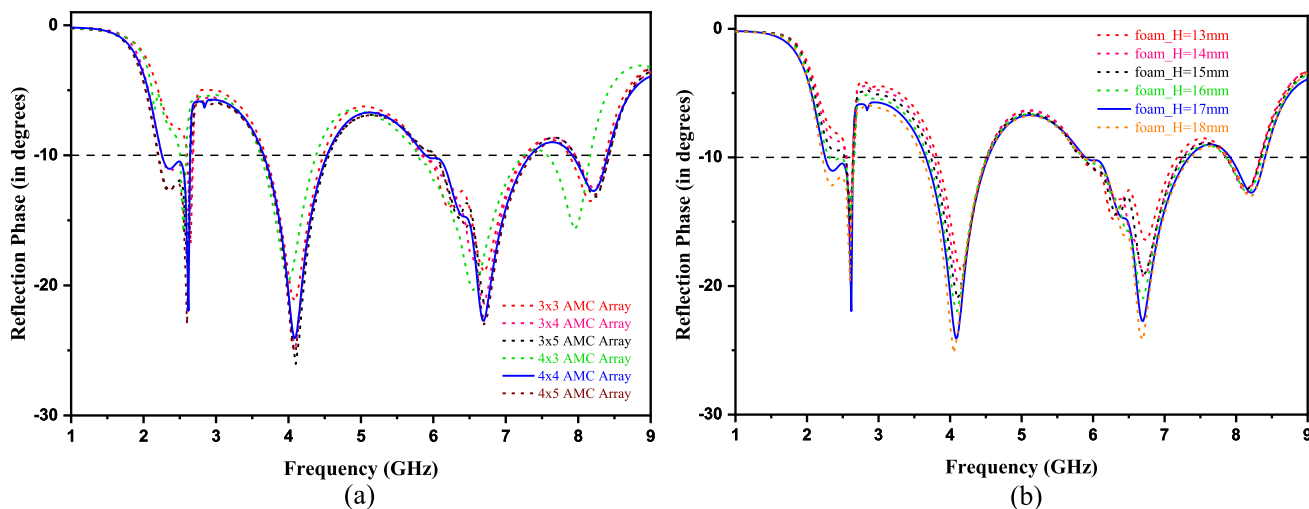


Fig. 23 Reflection coefficients of antenna for a variation in array size b variation in foam_H

Table 4 Realized gain (in dB) of the antenna for different AMC array sizes

AMC array sizes	Realized gain of the antenna integrated with AMC (in dB)		
	2.45 GHz	4.1 GHz	6.5 GHz
3 × 3	6	7.1	6.5
3 × 4	6.9	7.5	6.2
3 × 5	6.5	7.9	6.3
4 × 3	6.1	7.9	6.8
4 × 4	7.1	8.2	7.5
4 × 5	6.9	8.3	7.3

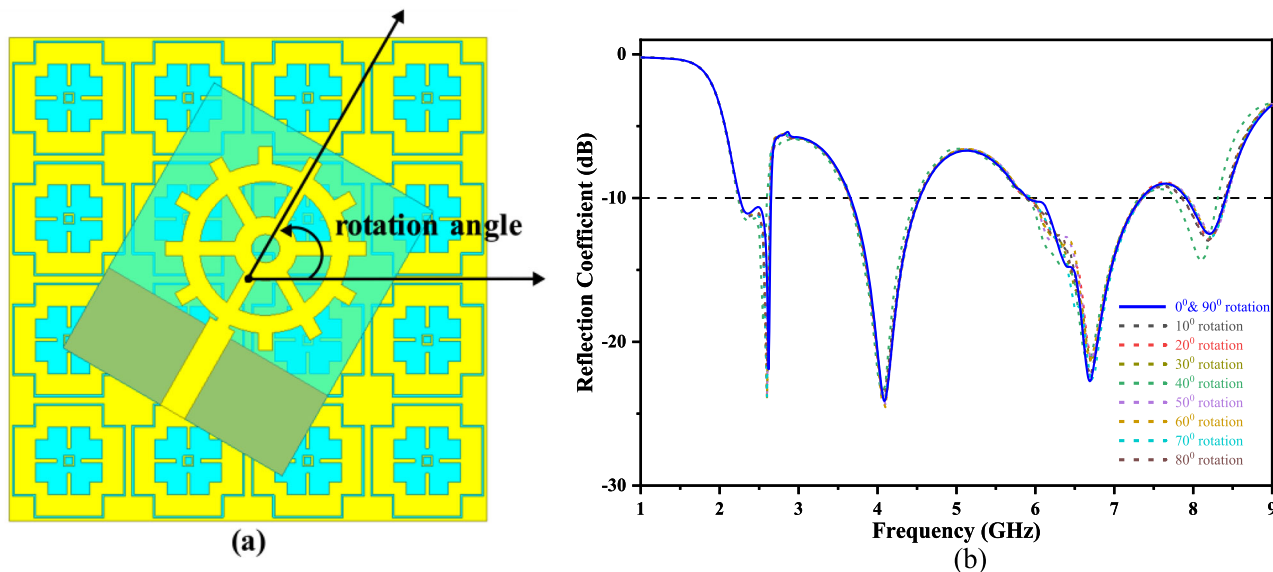


Fig. 24 a Top view of the antenna system with rotation angle and b S₁₁ of the antenna with different values of rotation angle

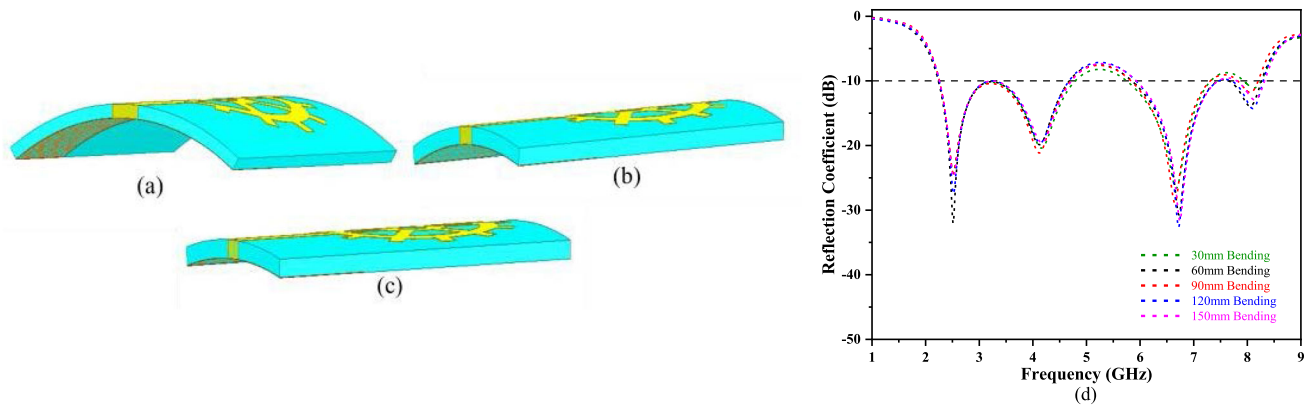


Fig. 25 Antenna curved on the cylindrical surface **a** 30 mm bending **b** 90 mm bending **c** 150 mm bending and **d** reflection coefficient for various bending

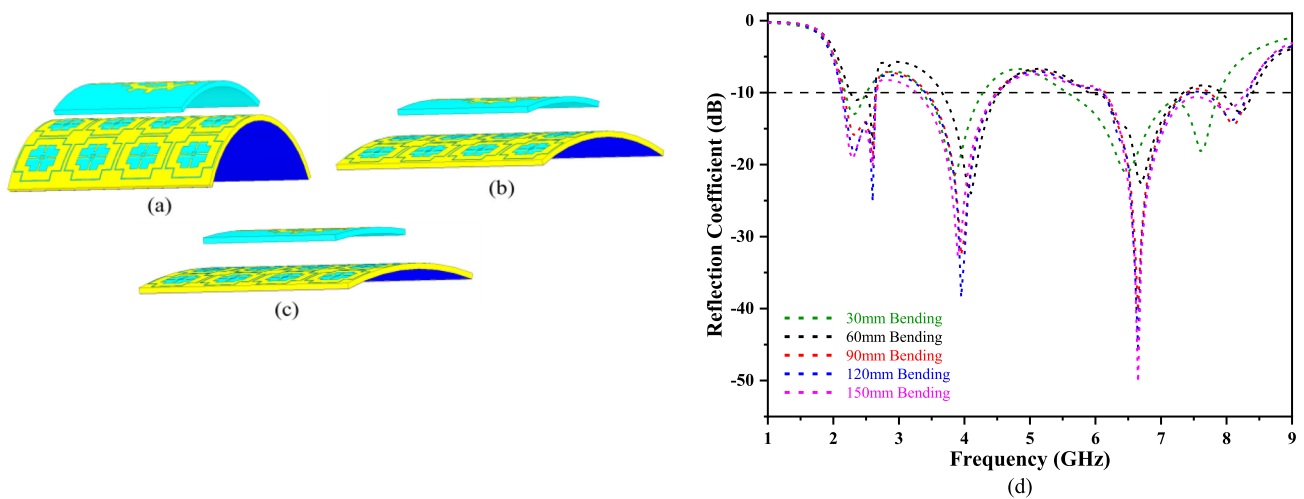


Fig. 26 Antenna with AMC curved on the cylindrical surface **a** 30 mm bending **b** 90 mm bending **c** 150 mm bending and **d** reflection coefficient for various bending

surface that blocks EM radiation from the back. Compared to the antenna without AMC, the maximum SAR value at 6.5 GHz is 0.25 W/kg, a reduction of 94.8% for an antenna with AMC. At all three resonant bands (2.45 GHz, 4.1 GHz, and 6.5 GHz), the SAR values for human tissues (hand, arm, and leg) from the antenna with AMC surfaces remain within the maximum limit set by the standard. Figure 27 presents a detailed comparison of SAR values. Comparisons between the performance of the proposed antenna and that of various existing antennas are presented in Table 5.

5 Conclusion

A compact, low-profile gear wheel-shaped antenna, supported by a 4 × 4 AMC array surface and designed to cover the ISM (2.4 GHz), C (3.7–4.2 GHz), and Wi-Fi 6E (5.9–7.1 GHz) bands, has been proposed. The perfect zero-

degree reflection phase characteristics at 2.45 GHz and 6.5 GHz have been achieved by the unit cell of the AMC, which can be attributed to its symmetry and DNG characteristics. The dimensions of the antenna are $0.294\lambda_0 \times 0.352\lambda_0 \times 0.013\lambda_0$ without AMC and $0.556\lambda_0 \times 0.556\lambda_0 \times 0.165\lambda_0$ with AMC. The antenna’s radiation performance was significantly improved by implementing AMC arrays of varying sizes. The sizes included 3 × 3, 3 × 4, 3 × 5, 4 × 3, 4 × 4, and 4 × 5, with the optimal results obtained with a 4 × 4 array. The antenna attained gains of 7.1 dBi at 2.45 GHz, 8.2 dBi at 4.1 GHz, and 7.5 dBi at 6.5 GHz, with impedance bandwidths of 18.4%, 21.2% and 22.3% for ISM, C, and Wi-Fi-6E bands, respectively. The integrated antenna design demonstrated the ability to achieve peak gains up to 8.2 dBi, FBR up to 25.2 dB, and efficiencies over 93%. A thorough investigation into the antenna’s bending behaviour concluded that a y-axis bend provided optimal functionality. Human tissues were utilized in the SAR

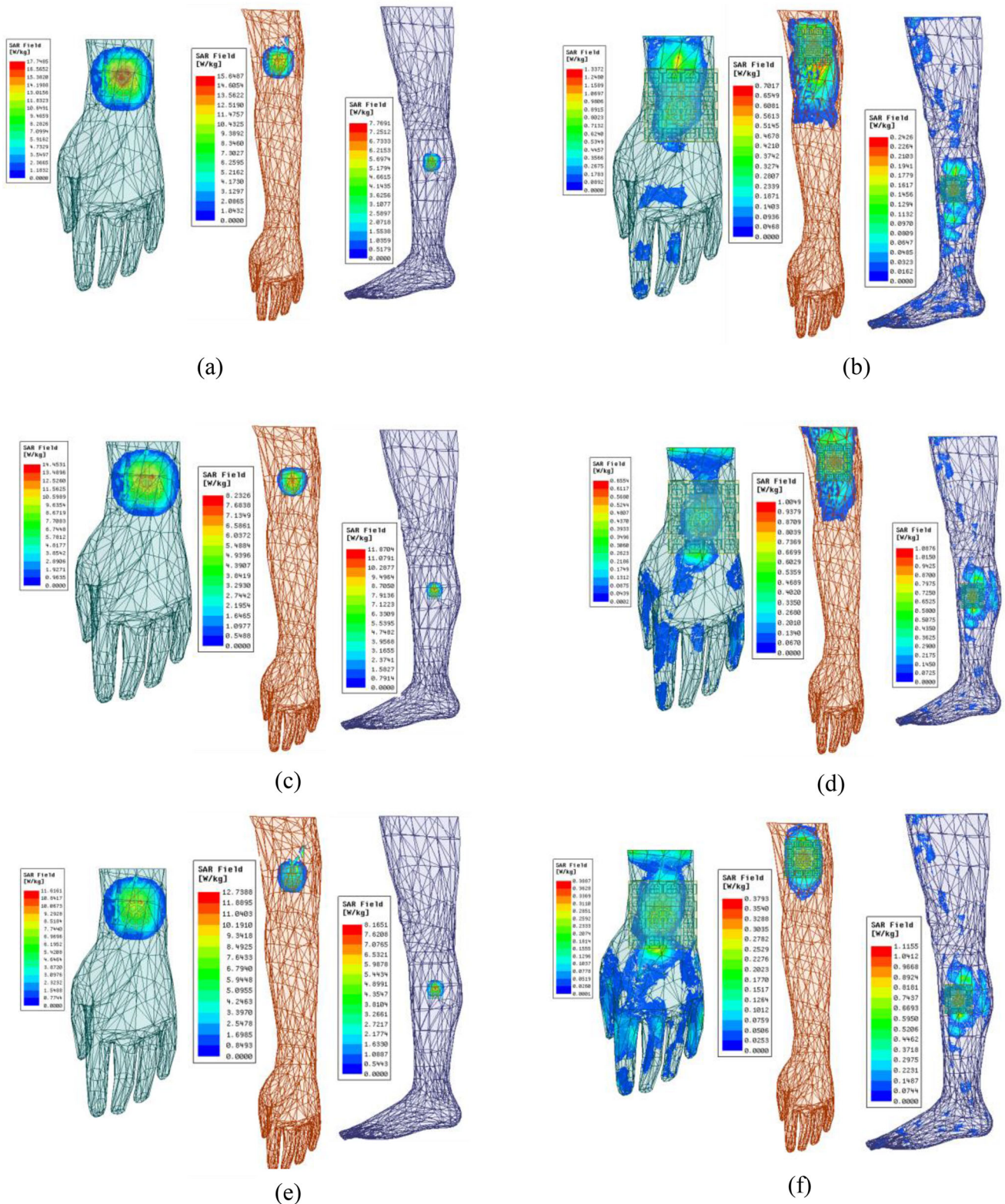


Fig. 27 SAR of the proposed antenna without AMC **a** 2.45 GHz **c** 4.1 GHz and **e** 6.5 GHz; with AMC **b** 2.45 GHz **d** 4.1 GHz and **f** 6.5 GHz

study at a distance of 5 mm from the antenna across all three frequency bands. At 2.45 GHz, 4.1 GHz, and 6.5 GHz, the maximum SAR values recorded were 1.3372

W/kg, 1.0076 W/kg, and 1.1155 W/kg, respectively, well below the FCC limit. ANSYS HFSS was used to simulate the antenna design, and the resulting antenna was

Table 5 Comparison of proposed antenna with existing antennas

References	Size of the antenna (mm ³)	Operating frequency/ band (GHz)	Gain (dBi)	FBR (dB)	SAR (W/kg)	Substrate material	AMC array size	Efficiency (%)
[9]	42 × 28 × 4	5.5	6.70	–	0.4317	Felt	3 × 2	77
[12]	80 × 80 × 1.6	0.95–2.11 3.05–5.39 5.84–8.19 9.14–10.68	4.56 2.28 4.26 4.30	–	–	FR4	–	–
[13]	62.65 × 62.65 × 5.65	2.4 3.9	7.9 8.6	5.6 12.2	0.021 0.043	FR4	2 × 2	> 90
[14]	33 × 33 × 6.75	2.9–12	3.24	9.159	0.083	FR4	4 × 4	75.38
[15]	50.7 × 25.7 × 7.1	2.4	6.76	–	0.406	Felt	3 × 3	88.4
[17]	30 × 30 × 11.25	6 8.4 10.3	8.24 10.6 9.6	7.3 18.6 9.7	0.203 0.212 0.217	FR4	2 × 2	> 90
[18]	66.8 × 66.8 × 5.5	2.45	7.47	> 20	0.15	Polyimide	2 × 2	–
[20]	86 × 86 × 20.3	3.5 5.8	9.1 7.7	25 23	0.0683 0.33	Rogers 3850	4 × 4	83.5 90.5
[21]	30 × 30 × 9.7	6.5 8.15	8.29 9.7	9.7 14.5	0.223 0.324	FR4	2 × 2	> 90
[22]	97.4 × 24 × 15.62	2.4	6.4	–	0.53	Medical transdermal patch	2 × 3	–
[23]	27 × 20 × 0.2	5.71–5.99	8.31	–	0.72	Polyimide	2 × 2	87
[30]	34.4 × 34.4 × 4.016	5.8	7.6	35.2	0.0264	RT/Duroid 5880	2 × 2	94.69
Proposed work	68 × 68 × 20.2	2.45 4.1 6.5	7.1 8.2 7.5	15.4 25.2 16.3	0.2426 0.6554 0.3793	FR4	4 × 4	> 93

fabricated. The antenna was tested in an Anechoic chamber using a VNA, and the measured results were consistent with the simulated results obtained using ANSYS HFSS. The proposed antenna design has the potential to be utilized in tri-band wireless applications, making it ideal for the next generation of consumer electronics. The experimental results demonstrate that the antenna's small size and high performance are well-suited for WBAN communications.

Data availability Data available on request from the authors.

Declarations

Conflict of interest No funding was received for this work, and the authors report no financial or personal conflict of interest. The manuscript isn't submitted to any other journals. This is only submitted to this journal.

References

- Chettri, L., & Bera, R. (2020). A comprehensive survey on internet of things (IoT) toward 5G wireless systems. *IEEE Internet of Things Journal*, 7(1), 16–32. <https://doi.org/10.1109/JIOT.2019.2948888>
- Mahmood, S. N., Ishak, A. J., Saeidi, T., Alsariera, H., Alani, S., Ismail, A., & Soh, A. C. (2020). Recent advances in wearable antenna technologies: A review. *Progress In Electromagnetics Research B*, 89, 1–27. <https://doi.org/10.2528/PIERB20071803>
- Mahmood, S. N., Ishak, A. J., Ismail, A., Soh, A. C., Zakaria, Z., & Alani, S. (2020). ON-OFF body ultra-wideband (UWB) antenna for wireless body area networks (WBAN): A review. *IEEE Access*, 8, 150844–150863. <https://doi.org/10.1109/ACCESS.2020.3015423>
- Jhang, W.-C., & Sun, J.-S. (2021). Small antenna design of triple band for WIFI 6E and WLAN applications in the narrow border laptop computer. *International Journal of Antennas and Propagation*, 2021, 1–8. <https://doi.org/10.1155/2021/7334206>
- FCC FACT SHEET. (2020). Unlicensed Use of the 6 GHz Band. Retrieved June 6, 2022, from [Online]. Available: <https://docs.fcc.gov/public/attachments/DOC-363490A1.pdf>
- Joshi, A., & Singhal, R. (2020). Probe-fed wideband AMC-integrated hexagonal antenna with uniform gain characteristics for

- WLAN applications. *Wireless Networks*, 26(5), 3569–3578. <https://doi.org/10.1007/s11276-020-02282-7>
7. Adel, Y. I., Ashyap, S. H., Dahlan, Z. Z., Abidin, M. R., Kamarudin, H. A., Majid, N. A., Mohammed Alduais, M., Dahri, H., & Alhandi, S. A. (2021). C-shaped antenna based artificial magnetic conductor structure for wearable IoT healthcare devices. *Wireless Networks*, 27(7), 4967–4985. <https://doi.org/10.1007/s11276-021-02770-4>
 8. Olatinwo, D. D., Abu-Mahfouz, A. M., & Hancke, G. P. (2021). A hybrid multi-class MAC protocol for IoT-enabled WBAN systems. *IEEE Sensors Journal*, 21(5), 6761–6774. <https://doi.org/10.1109/JSEN.2020.3037788>
 9. Gao, G.-P., Yang, C., Hu, B., Zhang, R.-F., & Wang, S.-F. (2019). A wearable PIFA with an All-Textile metasurface for 5 GHz WBAN applications. *IEEE Antennas and Wireless Propagation Letters*, 18(2), 288–292. <https://doi.org/10.1109/LAWP.2018.2889117>
 10. Wu, T., Wu, F., Qiu, C., Redoute, J.-M., & Yuce, M. R. (2020). A rigid-flex wearable health monitoring sensor patch for IoT-connected healthcare applications. *IEEE Internet of Things Journal*, 7(8), 6932–6945. <https://doi.org/10.1109/JIOT.2020.2977164>
 11. Liao, C.-T., Yang, Z.-K., & Chen, H.-M. (2021). Multiple integrated antennas for wearable fifth-generation communication and internet of things applications. *IEEE Access*, 9, 120328–120346. <https://doi.org/10.1109/ACCESS.2021.3107730>
 12. Liu, X., Wang, H., Yang, X., & Wang, J. (2022). Quad-band circular polarized antenna for GNSS, 5G and WIFI-6E applications. *Electronics*, 11(7), 1133. <https://doi.org/10.3390/electronics11071133>
 13. Hazarika, B., Basu, B., & Nandi, A. (2020). Design of antennas using artificial magnetic conductor layer to improve gain, flexibility, and specific absorption rate. *Microwave and Optical Technology Letters*, 62(12), 3928–3935. <https://doi.org/10.1002/mop.32531>
 14. Aitbar, I., Shoaib, N., Alomainy, A., Quddious, A., Nikolaou, S., Ali Imran, M., & H. Abbasi, Q. (2022). AMC Integrated Multi-layer Wearable Antenna for Multiband WBAN Applications. *Computers, Materials & Continua*, 71(2), 3227–3241. <https://doi.org/10.32604/cmc.2022.023008>
 15. El Atrash, M., Abdalla, M. A., & Elhennawy, H. M. (2021). A compact flexible textile artificial magnetic conductor-based wearable monopole antenna for low specific absorption rate wrist applications. *International Journal of Microwave and Wireless Technologies*, 13(2), 119–125. <https://doi.org/10.1017/S1759078720000689>
 16. Aun, N. F. M., Soh, P. J., Jamlos, M. F., Lago, H., & Al-Hadi, A. A. (2017). A wideband rectangular-ring textile antenna integrated with corner-notched artificial magnetic conductor (AMC) plane. *Applied Physics A*, 123(1), 19. <https://doi.org/10.1007/s00339-016-0619-1>
 17. Hazarika, B., Basu, B., & Nandi, A. (2021). Design of wideband AMC integrated monopole antenna with enhanced radiation performances for off-body systems. *Microwave and Optical Technology Letters*, 63(5), 1458–1463. <https://doi.org/10.1002/mop.32756>
 18. Yin, B., Gu, J., Feng, X., Wang, B., Yu, Y., & Ruan, W. (2019). A low SAR value wearable antenna for wireless body area network based on AMC structure. *Progress In Electromagnetics Research C*, 95, 119–129. <https://doi.org/10.2528/PIERC19040103>
 19. Li, E., Li, X. J., & Seet, B.-C. (2021). A triband slot patch antenna for conformal and wearable applications. *Electronics*, 10(24), 3155. <https://doi.org/10.3390/electronics10243155>
 20. El Atrash, M., Abdalla, M. A., & Elhennawy, H. M. (2019). A wearable dual-Band low profile high gain low SAR antenna AMC-backed for WBAN applications. *IEEE Transactions on Antennas and Propagation*, 67(10), 6378–6388. <https://doi.org/10.1109/TAP.2019.2923058>
 21. Hazarika, B., Basu, B., & Nandi, A. (2022). A wideband, compact, high gain, low-profile, monopole antenna using wideband artificial magnetic conductor for off-body communications. *International Journal of Microwave and Wireless Technologies*, 14(2), 194–203. <https://doi.org/10.1017/S1759078721000490>
 22. Othman, N., Samsuri, N. A., Mohamad, K. A., & Rahim, K. K. (2020). Low specific absorption rate and gain-enhanced meandered bowtie antenna utilizing flexible dipole-like artificial magnetic conductor for medical application at 2.4 GHz. *Microwave and Optical Technology Letters*, 62(12), 3881–3889. <https://doi.org/10.1002/mop.32507>
 23. Nadh, B. P., Madhav, B. T. P., Kumar, M. S., Anilkumar, T., Rao, M. V., & Kishore, P. V. V. (2020). Windmill-shaped antenna with artificial magnetic conductor-backed structure for wearable medical applications. *International Journal of Numerical Modelling: Electronic Networks, Devices and Fields*. <https://doi.org/10.1002/jnm.2757>
 24. Hazarika, B., Basu, B., & Nandi, A. (2020). An artificial magnetic conductor-backed monopole antenna to obtain high gain, conformability, and lower specific absorption rate for WBAN applications. *International Journal of RF and Microwave Computer-Aided Engineering*. <https://doi.org/10.1002/mmce.22441>
 25. Ran, M., Ye, M., & Yin, B. (2022). A dual-band ultra-wideband conformal antenna for WCE. *Progress In Electromagnetics Research M*, 111, 89–101. <https://doi.org/10.2528/PIERM22040401>
 26. Smith, D. R., Vier, D. C., Koschny, Th., & Soukoulis, C. M. (2005). Electromagnetic parameter retrieval from inhomogeneous metamaterials. *Physical Review E*, 71(3), 036617.
 27. Hadarig, R. C., de Cos, M. E., & Las-Heras, F. (2013). Novel miniaturized artificial magnetic conductor. *IEEE Antennas and Wireless Propagation Letters*, 12, 174–177. <https://doi.org/10.1109/LAWP.2013.2245093>
 28. Raad, H. R., Abbosh, A. I., Al-Rizzo, H. M., & Rucker, D. G. (2013). Flexible and compact AMC based antenna for tele-medicine applications. *IEEE Transactions on Antennas and Propagation*, 61(2), 524–531. <https://doi.org/10.1109/TAP.2012.2223449>
 29. Balanis, C. A. (2015). *Antenna theory: Analysis and design* (4th ed.). Wiley.
 30. Chaouche, Y. B., Nedil, M., Mabrouk, I. B., & Ramahi, O. M. (2022). A wearable circularly polarized antenna backed by AMC reflector for WBAN communications. *IEEE Access*, 10, 12838–12852. <https://doi.org/10.1109/ACCESS.2022.3146386>

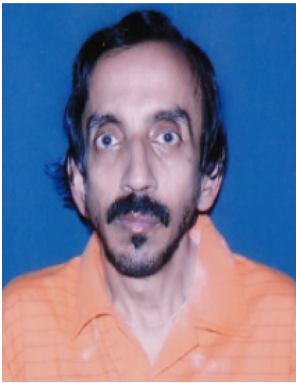
Publisher's Note Springer Nature remains neutral with regard to jurisdictional claims in published maps and institutional affiliations.

Springer Nature or its licensor (e.g. a society or other partner) holds exclusive rights to this article under a publishing agreement with the author(s) or other rightsholder(s); author self-archiving of the accepted manuscript version of this article is solely governed by the terms of such publishing agreement and applicable law.



V Rajavel received his M.E. degree in Communication and Networking in 2017 from Madras Institute of Technology Campus, Anna University, Chennai. Currently he is pursuing Ph.D. from National Institute of Technology, Agartala. He has 3.5 years of academic experience. His research interests are antenna design and networking.

optimization techniques, linear and non-linear optics (along with photonics) and opto-electronics, semiconductor physics and devices, and digital signal processing are among his research and teaching interests.



Dr. Dibyendu Ghoshal, received a Ph.D. (Tech) from Calcutta University's Institute of Radio Physics and Electronics in 1997. He has more than twelve years of teaching experience. He is the author of more than 150 research articles. At the National Institute of Technology, Agartala, he is an Associate Professor in the Electronics and Communication Engineering department. Microwave and millimetre wave technology and antenna engineering, digital

signal and image processing with associated soft computing and